Marine Geology
November 2012, Volumes 329–331, Pages 58–74
http://dx.doi.org/10.1016/j.margeo.2012.09.002

Distribution, morphology and triggers of submarine mass wasting in the Sea of Marmara

T.A.C. Zitter[a, *], C. Grall[a, f], P. Henry[a], M.S. Özeren[b], M.N. Çağatay[b], A.M.C. Şengör[b, c], L. Gasperini[d], B. Mercier de Lépinay[e], L. Géli[f]

[a] Aix Marseille Université, CNRS, Collège de France, IRD, CEREGE UMR7330, 13545 Aix-en-Provence cedex 4, France
[b] Istanbul Technical University, Department of Geology, Istanbul, Turkey
[c] Istanbul Technical University, Eurasia Institute of Earth Sciences, Istanbul, Turkey
[d] ISMAR, Italy
[e] Géoazur, CNRS, Université de Nice, IRD, OCA, Nice, France
[f] IFREMER, French Research Institute for Exploitation of the Sea, Brest, France

*: Corresponding author : T. A. C. Zitter, Tel.: + 33 4 42 38 14 61 ; email address : zitter@atgeo.fr

Abstract:

An overview is given of mass wasting features along the slopes of the Sea of Marmara, Turkey, based on new data and previously published information. The Sea of Marmara is characterized by active tectonics along the North Anatolian Fault and by eustatic sea level changes controlling the connections both to the Mediterranean and Black Sea (i.e. lacustrine and marine conditions during sea-level low and high stands, respectively). High resolution bathymetric data, subsurface echo-sounder and seismic reflection profiling, seafloor visual observations, as well as stratigraphic analysis of sediment cores have been used to identify, map and date submarine slope failures and mass wasting deposits. Gravity mass movements are widespread on the steep slopes of the Sea of Marmara, and range from small scale slope failures, mainly located within the canyons, to wider unstable areas (20 to 80 km^2). The largest mass wasting features, i.e. the Tuzla, Ganos and Yalova complexes, have been analyzed in connection with crustal deformation. These gravitational gliding masses are probably induced by the transtensional deformation within the crust. Moreover, age determination of landslides and debris flows indicate that they were more frequent during the last transgressive phase, when the rate of terrigenous sediments supplied by the canyons to the deep basin was higher. We discuss these results taking into account activity, pre-conditioning and trigger mechanisms for slope instability with respect to tectonics and paleo-environmental changes induced by sea-level oscillations.

Highlights

► We map mass wasting features in the Sea of Marmara. ► Climate change appears as one of the factor triggering slope instability. ► The biggest slides occur in areas of high micro-seismic activity. ► Underlying crustal deformation influence the distribution of slope instability.

Keywords: Sea of Marmara ; mass wasting ; seafloor morphology ; sea-level ; normal faulting

1. Introduction

Massive slope instabilities are very common on continental slopes. They control the seafloor morphology and have a substantial role in terms of natural hazards. Sediment mass wasting features are usually distinguished as instantaneous mass failures on the one hand (including rock avalanches, slides and slumps) and mass flows on the other hand, either cohesive (debris and mud flows) or non-cohesive (i.e. turbidity currents) (Coussot and Meunier, 1996 and Mulder and Cochonat, 1996). These distinctions reflect differences in the deformation processes, depending on the characteristics of the solid component and the water content. Although many types of mass movements are included in the general term “landslide”, submarine slides, either translational or rotational, should be restricted to consolidated material sliding above a slip or “decollement” surface. Creep is a particular type of mass flow defined by a very slow gravity-driven downward motion of slope caused by shear deformation (Flood et al., 1993, Lee and Chough, 2001 and Lee et al., 2002). Creep is associated with sediment waves on the seafloor, although these can also be related to other processes such as contourite or turbidity-currents (Lee et al., 2002). All of these processes generally grade into one another during transport, so that they may occur sequentially during a single destabilization event.

Little is known about triggers of deepwater failures. However, numerous studies demonstrate that the importance and recurrence of mass wasting on continental slopes depend on multiple factors such as lithology, structural inheritance, seismicity, tectonic activity, sedimentary input, eustatism, or fluid overpressure (Piper et al., 1997, Orange et al., 1999, Hovland et al., 2001, Leynaud et al., 2004,

53 Tripsanas et al., 2008; Mulder et al., 2009). Analysing mass wasting features morphology and
54 occurrence patterns yields insight into the processes that shape a particular margin and other
55 margins with similar settings.
56 Because the Sea of Marmara combines a high tectonic activity and drastic paleoenvironmental
57 changes, it is a highly favorable environment for studying submarine mass movement triggers. The
58 slopes of the Sea of Marmara, that have been intensively surveyed since the 1999 Izmit-Kocaeli
59 earthquake, display numerous morphological signs of recent mass wasting processes (Gazioğlu et al.,
60 2002; Görür and Çağatay, 2010; Özeren et al., 2010). This paper focuses on the various types of slope
61 instabilities participating in the shaping of the Sea of Marmara basins. First, we will give an overview
62 of the distribution, extent and timing of recent mass wasting features; then, based on the results of
63 an analysis carried out over a number of different cases in different sectors of the Sea of Marmara,
64 we will discuss the possible influence of tectonics and sea-level changes on triggering instabilities.
65
66 **2. Geological setting and previous studies**
67 *2.1. Structural and seismotectonic context*
68 The Sea of Marmara is located at a releasing bend along the single through-going westward
69 prolongation of the North Anatolian Fault (NAF), the Main Marmara Fault (MMF, Le Pichon et al.,
70 2001; Rangin et al., 2004). It comprises three main basins with rather steep slopes, from west to east
71 respectively: the Tekirdağ, Central and Çınarcık Basin, separated by two major structural highs, the
72 Western and Central Highs (Fig. 1). The MMF comprises more precisely three connected segments in
73 the Sea of the Marmara: the Tekirdağ Basin/Western High segment, the Istanbul segment extending
74 over the Central High, and the Çınarcık segments forming two major bends of the Main Marmara
75 Fault (Grall et al., 2012; Seeber et al., 2006). The extensional component of motion is partitioned
76 between oblique portions of the MMF and secondary fault branches (Şengör et al., 1985; Le Pichon
77 et al., 2001; Armijo et al., 2002; Le Pichon et al., 2003; Şengör et al., 2005). The Ganos bend (Seeber
78 et al., 2004) limits a western uplifted area, the Ganos Mountain, where thrusting is prominent

particularly onland (Yaltirak, 2002; Seeber et al., 2004), on to a southeastern subsiding area, the Tekirdağ Basin. At the eastern end, two bends can be described at either ends of the Çınarcık Basin: the Tuzla bend and the Istanbul bend (Seeber et al., 2006). Historical earthquake activity in the Sea of Marmara region is organized in sequences with a typical recurrence of 200-300 years (Ambraseys and Finkel, 1995; Ambraseys and Jackson, 1998; Ambraseys and Jackson, 2000; Yalciner et al., 2002; Parsons, 2004). Numerous micro-seismic studies focus on the Tuzla bend along the northern Çınarcık fault segment (Karabulut et al., 2002; Karabulut et al., 2003; Sato et al., 2004; Örgülü, 2011; Karabulut et al., 2011). This area still retains microseismic activity after the 1999 Izmit-Kocaeli earthquake, consisting mainly of normal fault aftershocks (Karabulut, 2002). Focal mechanisms indicate shallow normal faulting (5 to 10 km deep) and deeper strike-slip faulting (11-14km) (Karabulut et al., 2002).

Part of the extensional deformation is also accommodated by the South Transtensional Zone (STZ, Grall et al., 2012). This area comprises low-angle normal faults,that probably have been redistributing crustal stretching since the early stages of basin formation (i.e. 5-3.5 Ma) (Bécel et al., 2010; Grall et al., 2012). However, it is unclear whether these low angle faults are still active, except in the southern Central Basin where there is evidence of present day activity (Bécel et al., 2009; 2010).

2.2. Marine/lacustrine transition within the Sea of Marmara

The paleoceanographic history of the Sea of Marmara during the glacio-eustatic cycles exhibits several disconnections and reconnections with the Mediterranean Sea water circulation (Ryan et al., 1997; Aksu et al., 1999; Major et al., 2002; McHugh et al., 2008; Çağatay et al., 2000; 2009). The Holocene marine sedimentation is composed of homogeneous greenish silty mud and laminated sapropel containing coccoliths (notably *Braarudosphera sp.*) and benthic foraminifers typical of a low oxygen marine environment. During that period, sedimentation rates varied from 0.1 to 0.5 m/ka on the plateau and shelves (Çağatay et al., 2000) to a maximum of 3 m/ka in the deep basins (Stanley and Blanpied, 1980; Çağatay et al., 2000). The sedimentation rates may have been 2 to 3 times

105 higher in the lacustrine period (Çağatay et al. 2003). During the last glacial, the Sea of Marmara was a
106 brackish water lake (Aksu et al., 1999; Çağatay et al., 2000; Ryan et al., 2003; Zitter et al., 2008). The
107 brackish lacustrine sedimentation in the deep basins is characterized by grayish laminated and
108 banded sediments with locally dark reduced spots and pyrite. The fauna associated with the shallow
109 lacustrine/brackish waters are fresh water bivalves (*Dreissena sp.*), diatoms (*Stephanodiscus,*
110 *Aulacoseira, Diploneis, Cyclobella*), and ostracodes (*Leptocythers, Candona Angulata* adults and
111 juveniles). The transition from lacustrine to marine deposits is marked by a peak in carbonate
112 content (Reichel and Halbach, 2007; Vidal et al., 2010) and the presence of a sapropelic layers within
113 the marine sediments (Çağatay et al., 1999; 2000). The most recent reconnection is dated at 14.7 cal.
114 Ka BP (Vidal et al., 2010) and followed by a progressive transition towards marine conditions lasting
115 more than 1.5 ka (Reichel and Halbach, 2007; Çağatay et al., 2009; Vidal et al., 2010).

116 *2.3 Morpho-sedimentary context*

117 Within the Sea of Marmara, the sediments are dominated by terrigeneous infill composed of 75%
118 gravity-induced discrete events sedimentation (turbidites and mud/debris flow) intercalated with
119 25% hemipelagic deposits (Beck et al., 2007, Çağatay et al., 2000; Çağatay et al., 2003, Çağatay et al.,
120 2009). These events have been tentatively correlated with earthquakes or tsunamis (McHugh et al.,
121 2006; Beck et al., 2007; Hébert et al., 2005; McHugh et al., 2008; Çağatay et al., 2009). It is inferred
122 that the 1999 Izmit-Kocaeli earthquake, that produced a surface rupture reaching the western end of
123 the Gulf of Izmit (Gasperini et al., 2011), triggered mass wasting events (Polonia et al., 2002; Kuşçu et
124 al., 2005; Cagatay et al., in press). Within the Central Basin, Beck et al. (2007) identified a several
125 meters thick homogeneous transparent acoustic layer, named “homogenite” (Kastens and Cita,
126 1981), and composed of very fined-grained sediment likely re-suspended after a large mass-wasting
127 event, consequence of a tsunamigenic earthquake. This event that remobilized at least 0.6 km^3 of
128 sediment occurred ca. 15.5-16 cal. ka (Beck et al., 2007), pre-dating about 1ka before the lacustrine
129 to marine transition.

Numerous studies of the seafloor morphology of the Sea of Marmara identified sediment waves (Okay et al., 1999; Imren et al., 2001 and Shillington et al., 2012) and mass wasting features (e.g. (Gazioğlu et al., 2002; Altinok et al., 2003; Gazioğlu et al., 2005; Gökçeoğlu et al., 2009; Görür and Çağatay, 2010; Özeren et al., 2010). A large part of these studies focused on two main landslides: the Ganos Complex (Gazioğlu et al., 2002; Altinok et al., 2003; Gazioğlu et al., 2005) and the Tuzla Complex (Gazioğlu et al., 2002; Gazioğlu et al., 2005; Gökçeoğlu et al., 2009; Görür and Çağatay, 2010; Özeren et al., 2010).

The Tuzla Complex is located at the eastern end of the straight cliff bounding the Çınarcık Basin to the north, where Paleozoic bedrock outcrops along the headwall of the scarp (Özeren et al., 2010). According to the convexity of the upper part of the landslide and to the hummocky topography of the landslide, Gökçeoğlu et al. (2009) assumed that the Tuzla Complex is a deep-seated rotational landslide and proposed to relate it to the secondary NW-SE faults (Tur et al., 2007). One of the two cores recovered in this area by Özeren et al. (2010) reached the top of the debris flow which is composed of angular mudstone clasts within a sandy mud matrix, 60 cm below the marine/lacustrine boundary. The age of this debris flow is estimated ca. 17ka BP but the geometry of the deep-seated landslide beneath the sediments deposited in Çınarcık Basin suggests a much longer history spanning at least one glacial cycle (Özeren et al., 2010). The Ganos Complex is located at the southwestern end of the Tekirdag basin. The direction of sediment flow on the Ganos Complex has been investigated by Gazioğlu et al. (2002) who proposed a single flow line, with an E or ENE orientation. The occurrence of a detachment below the complex is suggested by the work of Okay et al. (1999).

Sediment wave fields occur in various places on the seafloor of the Sea of Marmara and have been investigated by different authors (Okay et al., 1999; Imren et al., 2001; Shillington et al., 2012) proposing different interpretations. More recently, a detailed analysis of these undulations, based on high resolution seismic data, concluded that these sediment waves correspond to slow gravity-driven downslope creep (Shilington et al., 2012).

156 **3. Identification of mass wasting areas: data and methods**

157 This study integrates marine datasets acquired during several cruises in the Sea of Marmara.
158 Morphological analysis is based on multibeam bathymetric and backscatter data. These data were
159 acquired from R/V Le Suroit during the Marmara Cruise in 2000 using a 30 kHz multibeam SIMRAD
160 EM300 system for which a Digital Elevation Model (DEM) with 38 m grid resolution was generated.
161 Shaded bathymetry and maps of slope gradient and slope aspect were automatically created using
162 the ArcGIS spatial analyst tool. Average slopes were determined within polygonal areas defined by a
163 similar slope along the margins of the main basins and on major submarine landslides (Tab. 1). High
164 resolution chirp profiling (with a hull-mounted 3.5 kHz echosounder) was obtained during the
165 Marmarascarps cruise in 2001 and the Marnaut cruise in 2007 on board R/V L'Atalante, and during
166 Marmara VT in 2004 on board the R/V Marion Dufresne. Manned submersible dives took place
167 during the Marnaut cruise (2007) with the submersible Nautile. Sediment cores were collected with
168 different sampling devices: a Kullenberg corer with a 10-m-long barrel on R/V L'Atalante (designated
169 with letters MNT) and with the giant Calypso piston corer on R/V Marion Dufresne (designated with
170 letters MD). MD cores were cut in sections of 1.5 m and MNT cores in sections of 1 m. X-ray
171 radiographs of several cores were obtained with the SCOPIX system of Bordeaux University to reveal
172 internal structures. Core MD042737 was also subsampled every 40 cm, around the supposed depth
173 of the marine/lacustrine transition (i.e. within the last 10 metres of the core), and these subsamples
174 were sieved and smear slides were made. Nanno fossils and diatoms were studied on the smear
175 slides. Other fossils were picked from the 150 μm fraction.

176 Mass wasting features can be identified from high resolution bathymetry (McAdoo et al., 2000).
177 Slides and slumps generally display sharp boundaries both upslope and downslope. They display
178 concave-downslope scar failures, with a steep headwall scarp (Fig. 2a). Mass flows (debris flows, mud
179 flows and turbidites) can be more difficult to identify in the bathymetric data when they lack clear
180 distal toes (Loncke et al., 2009b). In this case, high resolution seismic profiling, such as 3.5 kHz data,
181 correlated with piston coring data is necessary to constrain the basinal extension of the features. On

182 echo-sounder profiles, different echo-types can correspond to mass transport deposits (Fig. 2b). They
183 are often recognised as acoustically transparent facies, in seismic profiles, corresponding to a
184 homogeneous mud (homogenite) in cores. The homogenite is coupled with a basal coarse turbidite
185 having a sharp and often erosive base (Beck et al., 2007; Çağatay et al., in press) (Fig. 2c). Hyperbolic,
186 chaotic, and hummocky echo-characteristics can also correspond to deposits generated by mass
187 wasting processes (Damuth, 1980; Embley, 1980; Loncke et al., 2006; Loncke et al., 2009a; Loncke et
188 al., 2009b). Well-stratified continuous and parallel reflections that usually characterize pelagic and
189 hemipelagic sediments may also correspond to cyclic deposition by turbidity currents (Domzig et al.,
190 2009, Fig. 11 in Zitter et al. 2008). Proximal mass wasting features can display different lithologic
191 facies within cores (Fig. 2c) such as mixed sand and shell debris layers, lenses, and lithified or semi-
192 lithified mud pebbles (Embley, 1980).
193
194 **4. Results**
195
196 *4.1 Morphology and distribution of mass wasting features*
197 The slopes of the northern margin of the Sea of Marmara are generally steeper and less sedimented
198 than the southern ones (Fig. 3 and Tab. 1). The steepest slopes are located on the north-western side
199 of Tekirdağ Basin (Ganos slope) where the average gradient is 19° (Tab. 1), and on the northern and
200 southeastern sides of Çınarcık Basin, with 23° and 17° average gradients respectively. The Central
201 Basin exhibits slope gradients of 8° on average in the south and 11° in the north, and the southern
202 and northern sides of Tekirdağ Basin have slope gradients of 8° on average (Tab. 1).
203 Figure 3 presents a map of morphological evidence of slope instabilities and the network of canyons
204 in the Sea of Marmara. All submarine mass wasting features identified on the seafloor of the Sea of
205 Marmara in this study are also presented in Table 2 together with references to previous studies.
206 Slope instabilities are more common along the southern margin. Individual zones of instability range
207 from 0.5 to more than 100 km^2 in surface area (Tab. 2). The smallest features are associated with

steep canyon walls. The largest are observed along both flanks of the Çınarcık Basin and on the southern slopes of the Tekirdağ and Central Basins. The Central and the Western Highs both exhibit slope instabilities. Many relatively small-scale arcuate scars are observed in the Western High. On the Central High slopes facing both the Çınarcık Basin and the Kumburgaz Basin, two broad zones (features 24 and 25 on Fig. 3) are affected by regularly spaced steps. Within the Tekirdağ Basin, the majority of submarine mass wasting features are located along the southern sedimented slope (features 1 to 6) despite the northwestern edge being much steeper. The Central Basin exhibits smaller and fewer mass wasting and most of them are located on its southwestern side, in association with the more developed canyon pattern, and at the toe of the Western High (features 11 to 21). Only one landslide (feature 22; 24 km^2 in area) is observed in the northeastern part of the basin. Both northern and southern slopes of the Çınarcık flanks are affected by slope instabilities but the area they cover is wider in the south.

4.2 Characterisation of mass wasting features

4.2.1.Çınarcık Basin

The Tuzla Landslide Complex (feature 30 on Fig. 3, Fig. 4) exhibits a large curvilinear slope failure, 32 km^2 in area, with an amphiteatre-like shape. It can be divided into two distinct areas. The western part displays a well-defined headwall scarp on the upper slope with a total height drop of 250 to 300 m (Fig. 5) and an average slope of 21° (Tab. 1). Several linear features, and smaller scarps, are visible within the bathymetry in the western part of the landslide. Rotated blocks are seen in the seismic section (Fig. 5) down slope up to 3000 m away from the main scarp. This part of the slope failure should thus be classified as a rotational slide, although it is unclear whether it resulted from a single event. Seismic profiles (see Fig. 5) show that at least 250 m of sediments within the basin onlap the top of the main slide body. Even for a maximum sedimentation rate estimated at 7 mm/yr during the last glacial time (Seeber et al., 2006), this would correspond to a minimum age of 35 000 years.

A submersible dive upslope across the headwall scarp has shown lower Devonian black shales (Fig. 5) at 1100 m of water depth, implying that the slide affects the Palaeozoic basement of the Istanbul block and suggesting sliding surfaces may root in these black shales. The eastern part of the feature, separated by a NNE-SSW trending ridge, already described by Tur et al. (2007), consists of a rough seafloor, with an average slope of 14°. It exhibits small normal faults and erosional gullies.

Although less steep than the northern Çınarcık slope, the southern Çınarcık slope with an average slope of 11° is also affected by numerous instabilities (Fig. 4). The easternmost part of the slope exhibits the highest slope angle (around 17°); and a landslide complex of 21 km^2, hereafter called the Yalova Complex, affects the entire slope from the shelf break to the basin (feature 29 on Fig. 3, Fig. 6). Concave downslope crescent shaped scars and debris flows are recognizable upslope, as well as a rectilinear headwall scarp. Numerous erosional gullies are observed from the scarp down to the basin. The Yalova Complex is cut by left-lateral faults, oriented N340° (parallel to the slope direction) that displace the base of the slope stepwise (Fig. 6). The toe of the landslide was explored during a submersible dive: it shows an accumulation of blocks of various sizes as well as evidence for fluid expulsion. Broken pieces of authigenic carbonate crusts observed on the seafloor were up to 15 m high, associated with fluid seepages. Alignments of 3-4 m long black patches of reduced sediments, striking N310° in the slope direction, are seen in some places and appear to coincide with the location of the left lateral faults (Fig. 6). In this part of the slope there are also several recent small rock debris accumulations from rock avalanches that are not yet covered by hemipelagic sediments.

Between E28°50 and E29°10, the slope is affected by faults, perpendicular to the slope direction, forming a broad zone of 118 km^2 in area (feature 27 on Fig. 3, Fig. 4). This area is located above a deep-seated transtensional shear zone, and the deformation of the seafloor may result from a combination of slope failure and tectonic motion. In this latter case, the faults observed on the bathymetry probably correspond to en-échelon normal faults induced by the transtensional deformation (Géli et al., 2008). Along the northern toe of the Çınarcık slope, at the base of a steep

cliff of Palaeozoic sediments, fallen blocks varying sizes from tens of centimetres to metre size boulders and slabs are commonly observed to be covered by a 1 to 10 cm sediment blanket (Fig. 7).

4.2.2. Western High and Central Basin

At the toe of the eastern slope of the Western High, in the Central Basin, some acoustically transparent lenses are seen directly at the seafloor indicating recent deposition. A Nautile dive in this area found a layer of authigenic carbonate crusts that was outcropping locally at a water depth of 1200 m on a very steep slope. This observation indicates that sliding occurred, exhuming carbonate crusts formed by fluid seepage activity either within the sediments or at seafloor.

Mass wasting deposits were found also in cores MNTKS19 and MNTKS22 located in the NE corner of the Central Basin at the toe of a landslide (feature 22 on Fig. 3). Core MNTKS19 shows at 205 cm depth a 35 cm thick section of very fine sand with shell debris which could correspond to the distal part of a mass flow. At a depth of 230 cm, in core MNTKS22, a 40 cm-thick interval was found with mud clast, pebbles and deformed sandy lenses, possibly corresponding to the same event.

4.2.3.Tekirdağ Basin

The Ganos Complex is located at the eastern end of the Ganos fault rupture over an elliptical area of 85 km² (feature 1 on Fig. 3, Fig. 8). This feature, which extends from a water depth of 150 m to 1100 m, shows a complex morphology. The slope, with an average gradient of 5°, is affected by small step-like scarps and sediment waves, perpendicular to the slope dip, and presents a rough and hummocky topography. Chirp profile Marnaut 16, running across the slope, shows an acoustic facies characterized by regular hyperbolae (Fig. 8). Along the northern side of this large moving mass, several imbricated crescent-shaped scars (features 3 and 4 on Fig. 3) indicate multiple smaller scale events of gravity sliding in retrogressive sequence. These slope failures are located along the strike-slip fault trace, where the transpressional fault that lies along the base of the Ganos slope branches off the main strike-slip fault lying along the southern slope of the Tekirdağ Basin (Fig. 8). An arcuate

shaped scar and irregularities in the bathymetry suggest a debris flow occurred in the upper part of the slope (feature 2 on Fig. 3). Retrogressive slope failures can also be observed at the toe of the landslide complex.

Cores MD042737, MD042740 and MNTKS30, located at the mouth of a canyon in the Tekirdağ Basin (see core location in Fig. 9), contain several silty-turbidite sequences, coarse shelly sand layers, and thick sandy or muddy layers with clay pebbles and mud clasts interpreted as a debris flow (Fig. 10). This debris flow facies is found at depths varying between 200 and 600 cm (Fig. 10). Considering the average sedimentation since the lacustrine to marine transition in the cores, the debris flow may correspond to a single event that occurred during the Holocene marine episode, but could not be precisely dated. Several deeper coarser sand beds with abundant *Dreissena sp.* shells are observed within the cores MD042737 and MD042740. In core MD042737, the marine-lacustrine transition is deduced from observations of micro and nanno fossils (foraminifera, ostracodes, diatoms) with progressive salinization of the waters between 31.75 and 30.5 m (this depth has been corrected for gas expansion on the basis of observed holes/gaps in the core), corresponding to an average sedimentation rate of 2.5 m/ka during the marine period, including mass wasting deposits. Sediment cores have been correlated with 3.5 kHz echosounder data (Fig. 11). Strong reflections correspond to turbidite sequences containing multiple sand laminae, and to the top of a thick coarse shelly sand layer at the base of the core (around 30 m depth below seafloor at the MD042737 location, i.e. 0.4s twt, Fig. 11). Reflections within the lacustrine facies tend to be fuzzy, in contrast to the marine sedimentary sequence that exhibits a well layered acoustic facies (Fig. 11).

A buried transparent lens interbedded within the hemipelagic sediments and the turbidites could be distinguished in several 3.5 kHz echo-sounder profiles running across the toe of the slope on the SE flank of the Tekirdağ Basin (Fig. 2b, 8 and 10). According to its location, this mass wasting deposit could be related to an arcuate shaped slope failure observed on the NW side of the western High (Fig. 2a and feature 8 in Fig. 3). Following the marine/lacustrine transition depth to the west, we can observe that the transparent lens is located just on top of the strong reflector corresponding to the

coarse shelly sand bed. Thus, this large debris flow occurred during the lacustrine to marine transition or shortly afterwards (ca. 14 cal. Ka BP).

4.3. The canyon network: erosional features

We observed numerous canyons and erosional gullies cutting across the slopes and some of the structural highs, with direct pathways to the deep basins. Most canyons and their tributaries originate near the continental-shelf break and extend to the base of the continental slope. They usually have high reflectivity in the EM300 multibeam backscatter images (Fig. 1) potentially caused by the slope incision, the presence of coarse and/or heterogeneous material in the bottom of the thalweg or the increased seafloor roughness from erosion within the canyon (e.g. (Augustin et al., 1996; Kenyon et al., 2002; Lamarche et al., 2011). We observed areas within canyons with both relatively high backscatter (both flanks of the Central basin and southern flank of the Tekirdağ Basin) and lower backscatter (north of the Tekirdağ Basin and Çınarcık Basin) that may indicate differences in recent activity or in the nature of the sediments. Along the steepest slopes (NW Tekirdağ, NE and S Çınarcık) the canyons are straight, narrow (a few hundred meters wide) and short (1 to 2 km long). No levees are associated with these canyons suggesting that they are dominated by erosion. On gentler slopes (S Tekirdağ Basin and Central Basin), canyons are longer (up to 15 km), wider (1 to 3 km), and incise deeper (100 to 400 m). Steeper slopes are found at the head of the canyons (20 to 30°) and along the flanks (10 to 20°), whereas the bottom of the thalweg has 1 to 3° slopes. The channels have several branches that are often deflected, especially in the proximity of the major topographic highs. Meandering channels are exceptional. One such channel is observed flowing northward of Imralı Island towards the Central Basin ending in the Çınarcık Basin (Fig. 1), which constitute the submarine extension of the Kocasu. Arcuate submarine slide scars, observed on the walls of the canyons (Fig. 3 and 9), and scours in the bottom of the thalweg, indicate that erosion within the canyons contribute to the sediment input to the basins (Fig. 9). Canyon wall instability is observed, notably within the canyons located south of the Central Basin, on the southern side of the

Western Ridge. Profile Marnaut 16 (Fig. 9) crosses the mouths of two canyons that merge at the base of the slope. Acoustically transparent lens shaped bodies with 8 m maximum thickness are found in both canyons that are interpreted as debris flow deposits. On top of these bodies, stratified hemipelagic sediments reach 5m thickness in the western canyon and pinch out towards east. These observations indicate a decrease in the activity of the canyons after the deposition of the debris flow (Fig. 9); a conclusion also supported by the generally flat floor of canyons thalwegs, particularly at their mouths, which contrasts with the morphology of presently more active canyons.

5. Discussion

5.1. Influence of paleoenvironmental changes on mass wasting processes

Sea-level oscillation modulates the sediment supply and consequently the activation of gravity mass movements. Near the end of the lacustrine period, coarse shelly sand was transiting the shelf to the deep basin through the canyons. During the marine period, turbidite layers appear thinner and finer grained and a part of the sediment transfer occurs by muddy debris flow. Several authors (Beck et al., 2007; McHugh et al., 2008; Çağatay et al., 2009) also note that gravity flows such as turbidity currents were more frequent during the lacustrine stage than during the marine stage. Furthermore, seismoturbidites are more frequent during the lacustrine period, although this is unlikely to reflect a variation in seismic activity (McHugh et al., 2008).

The dating of mass wasting deposits indicates that the large mass wasting events occurred more frequently at the end of the last glacial period (12-17 ka). For example, the homogenite in the Central Basin is dated around 15.5-16 ka (Beck et al., 2007), and a mudflow on the larger Tuzla Complex is dated 17 ka by Özeren et al. (2010). However, this landslide complex appears to be a multi-event feature and older mass wasting deposits (probably as old as 35 ka) have been identified within the seismic section. By correlating the sedimentary facies and the different seismic horizons within the chirp profile in the Tekirdağ basin (Fig. 11), we have estimated that a large debris flow was deposited

362 during the lacustrine to marine transition or shortly afterwards (ca. 14 cal ka BP) (Fig. 9 and 11). We
363 also presented evidence here for variations in canyon activity for the case of the southern slope of
364 Tekirdağ Basin.
365 The observation of a -85 m paleoshoreline, notably on the northwestern part of the Izmit Gulf
366 (Çağatay et al., 2003), suggests that a large part of the present day shelves were exposed during the
367 last glaciation when the Sea of Marmara was disconnected from the Aegean Sea. During this low
368 stand, sedimentation rates were up to three times higher in the basins (Çağatay et al., 2000; Seeber
369 et al., 2006). We documented that the canyons were transferring coarse sandy material at that time.
370 It can be inferred that they were actively eroding and incising their own channels. The rapid sea-level
371 rise at the end of the last glaciation resulted in temporary sediment storage on the shelves and a
372 sudden decrease of sediment transfer through canyons by turbidity currents. The instability of the
373 recently incised canyon slopes caused debris flows, which still remain visible buried within several
374 canyons (Fig. 9). Afterward, sediment transfer by turbidity currents resumed, but with smaller fluxes.
375 We cannot rule out that gas hydrate dissociation as a consequence of warming during deglaciation
376 may have contributed to destabilization processes on the slope of the Sea of Marmara. Fluid ascent
377 is often thought to be the cause of sediment destabilization (Hovland et al., 2001; Mienert et al.,
378 2005). Numerous sites of fluid escape have been observed on the seafloor along the active fault
379 traces in the Sea of Marmara (Halbach et al., 2000; Armijo et al., 2005; Géli et al., 2008; Zitter et al.,
380 2008; Tryon et al., 2010) and gas hydrates were recovered within the subsurface sediments of the
381 Western High (Bourry et al., 2009). In this area, massive methane release occurred in the water-
382 column around 11 cal. ka BP, after the lacustrine to marine transition (Menot and Bard, 2010).
383 However, it is yet unclear whether this event was associated with an increase of slope instability.
384
385 *5.2. Influence of underlying crustal deformation on mass wasting processes*
386 The deep structure beneath the large landslides is not well resolved but the distribution of micro-
387 seismic activity (Sato et al., 2004; Karabulut et al., 2002; 2003; 2011; Örgülü, 2011) indicates active

388 crustal strain is occurring beneath these landslides. We argue that the slope instabilities observed at
389 a shallow level in the crust or within the sedimentary layers could be influenced by underlying crustal
390 deformation, as has also been proposed in the case of deep seated gravitational slope deformation
391 on land (e.g., Guglielmi and Cappa, 2009; Sanchez et al., 2010). Occurrence of large earthquakes on
392 major faults is an obvious trigger of instability, but distributed strain and fracturing could also
393 contribute to weaken the material above, eventually leading to catastrophic failure.

394 5.2.1. The Tuzla Landslide

395 Micro-seismic events in the Tuzla landslide area are oriented along two major trends: NE-SW and
396 ESE-WNW (Fig. 12). It is interesting to note that the NE-SW alignment coincides with the north-
397 western slope failure of the landslide (Karabulut et al., 2002; Sato et al., 2004; Karabulut et al., 2011),
398 but that strike of the nodal planes of the dominantly normal focal mechanisms is NW-SE (Fig. 12),
399 (Fig. 4 in Karabulut et al., 2002), implying en echelon faulting in agreement with the expected pattern
400 of faulting related to the northern branch of the North Anatolian Fault here, and with the dominant
401 morphological grain on the Thracian isthmus (Şengör, 2011). Within the Tuzla landslide, several linear
402 structures visible in the bathymetry also appear to coincide with alignments of micro-seismicity, as
403 far as the accuracy of micro-seismic event localization permits. The Tuzla micro-seismic cluster is
404 focused on the western triangular part of the Tuzla landslide, which is controlled by normal faulting,
405 whereas fewer seismic events occur eastward (Fig. 12). This suggests that the occurrence and
406 geometry of the landslide are controlled by active crustal structures.

407 5.2.2. The SE Çınarcık landslides: the Yalova Complex

408 Long term micro-seismic activity is present in a broader swath along the southern edge of Çınarcık
409 Basin, where numerous slope instabilities are observed (features 27, 29, 31, 32 on Fig. 3) and at the
410 entrance of the Izmit Gulf (Fig. 12). This area in particular displays a large mass of creeping sediments
411 (feature 32 on Fig. 3) extending over 12 km^2 and partially covering the fault trace near the end of the
412 1999 Izmit-Kocaeli earthquake rupture and the Yalova Complex (Fig. 6), (Gasperini et al., 2011).
413 Unsedimented chaotic blocks and associated active fluid seepages observed on the Yalova Complex,

attest to the recent activity of this landslide. Less than 10 km southward, the Armutlu Fault follows the northern shore of the Armutlu Peninsula (Parke et al., 1999; Armijo et al., 2002; Parke et al., 2002). This fault segment shows important micro-seismic activity, particularly in the vicinity of cities of Çınarcık and Yalova, with transtensional focal mechanisms (Fig. 4 in Karabulut et al., 2002; Sato et al., 2004; Karabulut et al. 2011, Örgülü, 2011). The northwestward gliding motion of the Yalova Complex may relate to the transtensional deformation, associated with the Armutlu fault.

5.2.3. The Ganos Landslide Complex

Micro-seismic activity is found on the Ganos fault, and along both the southern and NE margins of the Tekirdağ Basin (Örgülü, 2011; Tary et al., 2011). The instrumental seismicity data show micro-seismicity beneath the Ganos Complex area, for the time-period between 1986 and 1996 (Gürbüz et al., 2000), 1996 and 2000 (Sato et al., 2004; Örgülü, 2011), 2002 and 2006 (Örgülü, 2011). The recurrence of the micro-seismicity in this area suggests some kind of relationship between the creeping of the Ganos Complex and tectonic strain in the crust (Fig. 12). The focal mechanisms below the Ganos complex (see Fig. 11 in Örgülü, 2011) are normal and strike slip with a consistent NE-SW direction of extension and, on a cross-section cut along this NE-SW direction appear to deepen north-eastward from a very shallow depth at the edge of the complex to 10-15 km depth (Fig. 11 in Örgülü, 2011). This seismic activity could be related to sliding on a crustal detachment fault, dipping to the northeast beneath the Ganos Complex, and of comparable strike, dip and depth range as crustal detachments observed further east in multichannel data (Bécel et al., 2009; Grall et al., 2012).

The Ganos Landslide Complex generally slopes north-northeast (Fig. 8) and could indicate a global NE motion of the slide. We suspect a relationship between distributed transtensional deformation in the crust with shallow spreading and slope failure above.

Moreover, the Ganos Landslide Complex can be divided into two parts (Fig. 8): the southern part has a northeast trending slope averaging 5.6°; and the northern part has a steeper 9° northward trending slope. The boundary between the two-sub-landslides corresponds to the linear prolongation of the Ganos fault segment of the NAF (Fig. 8) where micro-seismicity with strike-slip focal mechanism is

observed (Örgülü, 2011). The seafloor expression of the NAF fault trace in the entrance to the Tekirdağ Basin is visible in the bathymetric data as a narrow furrow joining several mini-basins, where mass transport deposits have been recognised from cores and chirp profiling (McHugh et al., 2006). The deposition of mass transport deposits and homogenites has been related to an earthquake, presumably the 1912 Ganos earthquake (McHugh et al., 2006). Further east, within the Ganos Landslide Complex, the furrow marking the fault ends within an arcuate slump scar (Fig. 3, features 3 and 4). Down slope, in the prolongation of the fault segment, the bathymetry is marked by sigmoid waves, typical of dextral strike-slip deformation. These observations indicate that the Ganos Landslide Complex is underlain by a blind segment of the NAF. Moreover, the fault bend is smoother in the basin than previously proposed because the Ganos Landslide Complex obscures the trace of the fault (Okay et al., 2004). As a consequence, the strike-slip motion is probably distributed between the NW front and the bulk of the creeping sedimentary mass. The deformation associated with the NAF may be responsible for the destabilization of the NW slope where numerous slumps and slide scars are observed.

5.2.4. Role of transtensional deformation

The location of large unstable slopes (i.e. Ganos, Tuzla and Yalova complexes), above seismically active transtensional structures suggest a relationship between crustal transtension and the observed deformation at the seafloor. However, most of the micro-earthquake hypocenters in these areas are located at a deeper level (5 km on average, with a 1-10 km range) than the slope instabilities, as the suspected sliding surfaces are never deeper than 1.5 km (Yaltirak, 2002; Rangin et al., 2004) and often much shallower (see seismic profile Fig. 5). We propose that the component of stretching imposed by crustal deformation promotes tensional fracturing of the rock mass leading to failure of the overlying sediments. This type of relationship has been demonstrated on land where long lasting and diffuse deformation coexists with volumetrically smaller but sometimes catastrophic failure events (Brückl et al. 2005; Guglielmi and Cappa, 2009; Sanchez et al., 2010). In the Sea of Marmara, the tectonic stress field can induce both strain softening and topography, and promote

466 long lasting deep seated gravitational slope deformation which in turn promotes occasional short-
467 lasting and shallower mass movements. As a result, slopes adjacent to releasing bends or within
468 transtensional areas may be more prone to slope failure than those near segments where the
469 deformation is almost pure strike-slip and concentrated in a narrow fault zone.
470
471 **6. Conclusion**
472 Mapping mass wasting features in the Sea of Marmara demonstrates the widespread occurrence of
473 slope instabilities. The Sea of Marmara indeed presents favorable conditions for submarine mass
474 movement, with high sedimentation rates, dominated by silico-clastic deposits, drastic paleo-
475 environemental changes (marine/lacustrine conditions) caused by global sea-level oscillations
476 enhanced by a peculiar physiography (the Dardanelles and the Bosphorous sills), and active tectonic
477 deformations maintaining very steep slopes ranging from 4 to 24 ° on average.
478 Submarine mass movements are observed along about 30% of these slopes over a total area of more
479 than 500 km^2. A diversity of mass wasting processes occurs as mainly landslides, mass flows and
480 creep. We can distinguish gravity slides related to erosional processes within the canyons, initiated
481 from the head walls and the incised channels of the canyons from wider unstable slopes that appear
482 associated with transtensional crustal deformation evidenced from microseismicity. These unstable
483 slopes display creeping down slope motion component, with a direction of motion coincident with
484 the underlying crustal stretching. The stretching of the crust probably promotes strain softening
485 within the shallow crust and sedimentary cover and large scale deep seated gravitational slope
486 deformation. On the other hand, the vertical component of slip along the main faults contributes to
487 steepen the slopes and consequently favors slope instability. This combination of factors may
488 account for the observed concentration of large landslides near fault bends.
489 Cyclic sea level variations also influence the mass wasting processes. Several mass wasting deposits
490 observed in the sedimentary record appear to date back 11-17ka BP, i.e. corresponding to the end of
491 the lacustrine period and the early marine period. Morphological observations and high resolution

profiling of the canyons also indicate variations in the rate of sediment transfer processes over the same time interval.

This study highlights that landslide triggering is dependent on contextual factors that influence the probability of occurrence of slope instabilities in space and time, for instance, the distribution of crustal stress and strain, paleo-environmental conditions and sea-level change.

Acknowledgments

We acknowledge the Captain, crew and technical staff of IFREMER-Genavir's R/V L'Atalante and of submersible Nautile, as well as the onboard scientific party, for their involvement during the Marnaut cruise. We also acknowledge the very efficient help of the Turkish Navy during this cruise. Financial support was provided by the "Agence Nationale de la Recherche" (project ISIS-ANR05-Catt-005-01) and we thank Nabil Sultan who led the ISIS program. This work was carried out within the framework of the European Seas Observatory Network of Excellence (ESONET NoE) funded through the European Commission's Sixth Framework Programme under the priority 'sustainable Development; Global Change and Ecosystems'. We acknowledge Jean-Luc Schneider, Brice Ferger and Joël Saint-Paul (University of Bordeaux) for their work on SCOPIX measurements. We thank Luc Beaufort, Christine Pailles, Laetitia Licari, and Hélène Bruneton (CEREGE) for their help identifying biomarkers in the Sea of Marmara sediments. AMC Şengör records his gratitude to the Turkish Academy of Sciences for support. We thank John Woodside for his help on improving the English writing of this manuscript. We thank two anonymous reviewers for their constructive comments that improved this manuscript.

References

517 Aksu, A.E., Hiscott, R.N.,Yasar, D., 1999. Oscillating Quaternary water levels of the Marmara Sea and
518 vigorous outflow into the Aegean Sea from the Marmara Sea Black Sea drainage corridor.
519 Marine Geology, 153(1-4), 275-302.
520 Altinok, Y., Alpar, B.,Yaltirak, C., 2003. Sarkoy-Murefte 1912 Earthquake's Tsunami, extension of the
521 associated faulting in the Marmara Sea, Turkey. Journal of Seismology, 7(3), 329-346.
522 Ambraseys, N., N.,Finkel, C.F., 1995. The seismicity of Turkey and adjacent areas, a historical review,
523 1500-1800. Eren, Istanbul, 240 pp.
524 Ambraseys, N.N.,Jackson, J.A., 1998. Faulting associated with historical and recent earthquakes in the
525 Eastern Mediterranean region. Geophys. J. Int., 133, 390-406.
526 Ambraseys, N.N.,Jackson, J.A., 2000. Seismicity of the Sea of Marmara (Turkey) since 1509. Geophys.
527 J. Int., 141, F1-F6.
528 Armijo, R., Meyer, B., Navarro, S.,King, G., 2002. Asymetric slip partitioning in the Sea of Marmara
529 pull-apart : a clue to propagation processes of the North Anatolian Fault? Terra Nova, 13, 80-
530 86.
531 Armijo, R., Pondard, N., Meyer, B., Uçarkuş, G., de Lépinay, B.M., Malavieille, J., Dominguez, S.,
532 Gutscher, M.A., Schmidt, S., Beck, C., Çağatay, N., Cakir, Z., Imren, C., Eris, K., Natalin, B.,
533 Ozalaybey, S., Tolun, L., Lefevre, I., Seeber, L., Gasperini, L., Rangin, C., Emre, O.,Sarikavak, K.,
534 2005.Submarine fault scarps in the Sea of Marmara pull-apart (North Anatolian Fault):
535 Implications for seismic hazard in Istanbul. Geochemistry, Geophysics and Geosystemes, 6,
536 Q06009, doi:10.1029/2004GC000896.
537 Augustin, J.M., LeSuave, R., Lurton, X., Voisset, M., Dugelay, S.,Satra, C., 1996. Contribution of the
538 multibeam acoustic imagery to the exploration of the sea-bottom. Marine Geophysical
539 Researches, 18(2-4), 459-486.
540 Bécel, A., Laigle, M., de Voogd, B., Hirn, A., Taymaz, T., Galve, A., Shimamura, H., Murai, Y., Lepine,
541 J.C., Sapin, M.,Ozalaybey, S., 2009. Moho, crustal architecture and deep deformation under

the North Marmara Trough, from the SEISMARMARA Leg 1 offshore-onshore reflection-refraction survey. Tectonophysics, 467(1-4), 1-21, doi:10.1016/j.tecto.2008.10.022.

Bécel, A., Laigle, M., de Voogd, B., Hirn, A., Taymaz,T., Yolsal-Cevikbilen, S., Shimamura, H., 2010. North Marmara Trough architecture of basin infill, basement and faults, from PSDM reflection and OBS refraction seismics. Tectonophysics, 490, 1–2, 1-14, doi: 10.1016/j.tecto.2010.04.004.

Beck, C., Mercier de Lépinay, B., Schneider, J.L., Cremer, M., Çağatay, N., Wendenbaum, E., Boutareaud, S., Menot, G., Schmidt, S., Weber, O., Eris, K., Armijo, R., Meyer, B., Pondard, N.,Gutscher, M.A., 2007. Late Quaternary co-seismic sedimentation in the Sea of Marmara's deep basins. Sedimentary Geology, 199(1-2), 65-89, doi: 10.1016/j.sedgeo.2006.12.031.

Bourry, C., Chazallon, B., Charlou, J.L., Donval, J.P., Ruffine, L., Henry, P., Géli, L., Çağatay, M.N., Inan, S.,Moreau, M., 2009. Free gas and gas hydrates from the Sea of Marmara, Turkey Chemical and structural characterization. Chemical Geology, 264(1-4), 197-206, doi: 10.1016/j.chemgeo.2009.03.007.

Brückl, E.,Parotidis, M., 2005. Prediction of slope instabilities due to deep-seated gravitational creep. Natural Hazards and Earth System Sciences, 5(2), 155-172.

Çağatay, M.N., Algan, O., Sakinc, M., Eastoe, C.J., Egesel, L., Balkis, N., Ongan, D.,Caner, H., 1999. A mid-late Holocene sapropelic sediment unit from the southern Marmara sea shelf and its palaeoceanographic significance. Quaternary Science Reviews, 18(4-5), 531-540.

Çağatay, M.N., Eris, K., Ryan, W.B.F., Sancar, U., Polonia, A., Akcer, S., Biltekin, D., Gasperini, L., Görür, N., Lericolais, G.,Bard, E., 2009. Late Pleistocene-Holocene evolution of the northern shelf of the Sea of Marmara. Marine Geology, 265(3-4), 87-100, doi: 10.1016/j.margeo.2009.06.011.

Çağatay, M.N., Görür, N., Algan, O., Eastoe, C., Tchapalyga, A., Ongan, D., Kuhn, T.,Kuşçu, I., 2000. Late Glacial-Holocene palaeoceanography of the Sea of Marmara: timing of connections with the Mediterranean and the Black Seas. Marine Geology, 167(3-4), 191-206.

568 Çağatay, M.N., Görür, N., Polonia, A., Demirbag, E., Sakinc, M., Cormier, M.H., Capotondi, L.,
569 McHugh, C., Emre, O.,Eris, K., 2003. Sea-level changes and depositional environments in the
570 Izmit Gulf, eastern Marmara Sea, during the late glacial-Holocene period. Marine Geology,
571 202(3-4), 159-173.
572 Çagatay, M.N., Erel.,L., Belucci, L.G., Polonia, A., Gasperini, L., Eris, E., Sancar, U., Biltekin, D., Ucarkus,
573 G., Ulgen, U.B., Damci, E. Sedimentary earthquake records in the Izmit Gulf, Sea of Marmara,
574 Turkey. Sedimentary Geology (in press).
575 Coussot, P.,Meunier, M., 1996. Recognition, classification and mechanical description of debris flows.
576 Earth-Science Reviews, 40(3-4), 209-227, doi:10.1016/0012-8252(95)00065-8.
577 Damuth, J.E., 1980. Use of high-frequency (3.5-12 kHz) echograms in the study of near-bottom
578 sedimentation processes in the deep-sea: A review. Marine Geology, 38(1-3), 51-75.
579 Domzig, A., Gaullier, V., Giresse, P., Pauc, H., Deverchere, J.,Yelles, K., 2009. Deposition processes
580 from echo-character mapping along the western Algerian margin (Oran-Tenes), Western
581 Mediterranean. Marine and Petroleum Geology, 26(5), 673-694, doi:
582 10.1016/j.marpetgeo.2008.05.006.
583 Embley, R.W., 1980. The role of mass transport in the distribution and character of deep-ocean
584 sediments with special reference to the North Atlantic. Marine Geology, 38(1-3), 23-50.
585 Flood, R.D., Shor, A.N.,Manley, P.L., 1993. Morphology of Abyssal Mudwaves at Project Mudwaves
586 Sites In The Argentine Basin. Deep-Sea Research Part II-Topical Studies in Oceanography,
587 40(4-5), 859-888, doi:10.1016/0967-0645(93)90038.
588 Gasperini, L., Polonia, A., Bortoluzzi, G., Henry, P., Le Pichon, X., Tryon, M., Cagatay, N.,Geli, L., 2011a.
589 How far did the surface rupture of the 1999 Izmit earthquake reach in Sea of Marmara?
590 Tectonics, 30, 11, doi:Tc10.1010.1029/2010tc002726.
591 Gazioğlu, C., Gokasan, E., Algan, O., Yucel, Z., Tok, B.,Dogan, E., 2002. Morphologic features of the
592 Marmara Sea from multi-beam data. Marine Geology, 190(1-2), 397-420.

593 Gazioğlu, C., Yucel, Z.Y.,Dogan, E., 2005. Morphological features of major submarine landslides of
594 Marmara Sea using multibeam data. Journal of Coastal Research, 21(4), 664-673, doi:
595 10.2112/03-0060.1.
596 Géli, L., Henry, P., Zitter, T., Dupre, S., Tryon, M., Çağatay, M.N., de Lépinay, B.M., Le Pichon, X.,
597 Şengör, A.M.C., Görür, N., Natalin, B., Uçarkuş, G., Oezeren, S., Volker, D., Gasperini, L.,
598 Burnard, P., Bourlange, S.,Party, M.S., 2008. Gas emissions and active tectonics within the
599 submerged section of the North Anatolian Fault zone in the Sea of Marmara. Earth and
600 Planetary Science Letters, 274(1-2), 34-39, doi: 10.1016/j.epsl.2008.06.047.
601 Gökçeoğlu, C., Tunusluoglu, M.C., Gorum, T., Tur, H., Gokasan, E., Tekkeli, A.B., Batuk, F.,Alp, H.,
602 2009. Description of dynamics of the Tuzla Landslide and its implications for further
603 landslides in the northern slope and shelf of the Cinarcik Basin (Marmara Sea, Turkey).
604 Engineering Geology, 106(3-4), 133-153, doi:10.1016/j.enggeo.2009.02.007.
605 Görür, N.,Çağatay, M.N., 2010. Geohazards rooted from the northern margin of the Sea of Marmara
606 since the late Pleistocene: a review of recent results. Natural Hazards, 54(2), 583-603, doi:
607 10.1007/s11069-009-9469-x.
608 Guglielmi, Y.,Cappa, F., 2010. Regional-scale relief evolution and large landslides: Insights from
609 geomechanical analyses in the Tinee Valley (southern French Alps). Geomorphology, 117(1-
610 2), 121-129, doi:10.1016/j.geomorph.2009.11.016.
611 Grall, C., Henry, P., Tezcan, D., Lépinay, B.M.d., Bécel, A., Géli, L., Rudkiewicz, J.-L., Zitter,
612 T.,harmégnies, F., 2012. Heat flow in the sea of Marmara Central Basin, possible implications
613 for the tectonic evolution of the North Anatolian fault. Geology (in press),
614 doi:10.1130/G32192.1
615 Gürbüz, C., Aktar, M., Eyidogan, H., Cisternas, A., Haessler, H., Barka, A., Ergin, M., Turkelli, N., Polat,
616 O., Ucer, S.B., Kuleli, S., Baris, S., Kaypak, B., Bekler, T., Zor, E., Bicmen, F.,Yoruk, A., 2000. The
617 seismotectonics of the Marmara region (Turkey): results from a microseismic experiment.
618 Tectonophysics, 316(1-2), 1-17.

619 Halbach, P., Kuşçu, I., Kuhn, T., Pekdeger, A.,Seifert, R., 2000. Methane in sediments of the deep
620 Marmara Sea and its relation to local tectonic structures (abstract). In: N. Görür (Editor),
621 NATO advanced Research Seminar: integration of earth sciences research on the 1999
622 Turkish and Greek earthquakes and needs for future cooperative research. Tubitak, Istanbul,
623 pp. 74.
624 Hébert, H., Schindele, F., Altinok, Y., Alpar, B.,Gazioğlu, C., 2005. Tsunami hazard in the Marmara Sea
625 (Turkey): a numerical approach to discuss active faulting and impact on the Istanbul coastal
626 areas. Marine Geology, 215(1-2), 23-43, doi: 10.1016/j.margeo.2004.11.006.
627 Hovland, M., Orange, D., Bjorkum, P.A.,Gudmestad, O.T., 2001. Gas hydrate and seeps - Effects on
628 slope stability: The "hydraulic model". Proceedings of the Eleventh (2001) International
629 Offshore and Polar Engineering Conference, Vol I, 471-476.
630 Imren, C., Le Pichon, X., Rangin, C., Demirbag, E., Ecevitoglu, B.,Görür, N., 2001. The North Anatolian
631 Fault within the Sea of Marmara : a new interpretation based on multi-channel seismic and
632 multi-beam bathymetry data. Earth Planet. Sci. Lett., 186, 143-158.
633 Karabulut, H., Bouin, M.P., Bouchon, M., Dietrich, M., Cornou, C.,Aktar, M., 2002. The seismicity in
634 the eastern Marmara Sea after the 17 August 1999 Izmit earthquake. Bulletin of the
635 Seismological Society of America, 92(1), 387-393.
636 Karabulut, H., osalabey, S., Taymaz, T., Aktar, M., Selvi, O.,Kocaoglu, A., 2003. A tomographic image
637 of the shallow crustal structure in the Eastern Marmara. Geophys. Res. Lett., 30, 2277.
638 Karabulut, H., Schmittbuhl, J., Ozalaybey, S., Lengline, O., Komec-Mutlu, A., Durand, V., Bouchon, M.,
639 Daniel, G.,Bouin, M.P., 2011. Evolution of the seismicity in the eastern Marmara Sea a
640 decade before and after the 17 August 1999 Izmit earthquake. Tectonophysics, 510(1-2), 17-
641 27, doi:10.1016/j.tecto.2011.07.009.
642 Kastens, K.A., Cita, M.B., 1981. Tsunami-induced transport in the abyssal Mediterranean Sea.
643 Geological Society of America Bulletin, 92, 845-857.

644 Kenyon, N.H., Klaucke, I., Millington, J.,Ivanov, M.K., 2002. Sandy submarine canyon-mouth lobes on
645 the western margin of Corsica and Sardinia, Mediterranean Sea. Marine Geology, 184(1-2),
646 69-84.
647 Kuşçu, I., Okamura, M., Matsuoka, H., Gokasan, E., Awata, Y., Tur, H.,Simsek, M., 2005. Seafloor gas
648 seeps and sediment failures triggered by the August 17, 1999 earthquake in the Eastern part
649 of the Gulf of Izmit, Sea of Marmara, NW Turkey. Marine Geology, 215, 193-214.
650 Lamarche, G., Lurton, X., Verdier, A.L.,Augustin, J.M., 2011. Quantitative characterisation of seafloor
651 substrate and bedforms using advanced processing of multibeam backscatter-Application to
652 Cook Strait, New Zealand. Continental Shelf Research, 31(2), S93-S109,
653 doi:10.1016/j.csr.2010.06.001.
654 Lee, H.J., Syvitski, J.P.M., Parker, G., Orange, D., Locat, J., Hutton, E.W.H.,Imran, J., 2002.
655 Distinguishing sediment waves from slope failure deposits: field examples, including the
656 'Humboldt slide' and modelling results. Marine Geology, 192(1-3), 79-104, doi:Pii S0025-
657 3227(02)00550-9.
658 Lee, S.H., Chough, S.K., 2001. High-resolution (2-7 kHz) acoustic and geometric characters of
659 submarine creep deposits in the South Korea Plateau, East Sea. Sedimentology, 48(3), 629-
660 644, doi:10.1046/j.1365-3091.2001.00383.x.
661 Le Pichon, X., Chamot-Rooke, N., Rangin, C., Şengör, A.M.C., 2003. The North Anatolian Fault in the
662 Sea of Marmara. Journal of Geophysical Research, 108, 2179, doi:101029/2002JB001862.
663 Le Pichon, X., Şengör, A.M.C., Demirbag, E., Rangin, C., Imren, C., Armijo, R., Görür, N., Çağatay, N.,
664 Mercier de Lépinay, B., Meyer, B., Saatcilar, R.,Tok, B., 2001. The active main Marmara fault.
665 Earth Planet. Sci. Lett., 192, 595-616.
666 Leynaud, D., Mienert, J.,Nadim, F., 2004. Slope stability assessment of the Helland Hansen area
667 offshore the mid-Norwegian margin. Marine Geology, 213(1-4), 457-480, doi:DOI
668 10.1016/j.margeo.2004.10.019.

669 Loncke, L., Droz, L., Gaullier, V., Basile, C., Patriat, M.,Roest, W., 2009a. Slope instabilities from echo-
670 character mapping along the French Guiana transform margin and Demerara abyssal plain.
671 Marine and Petroleum Geology, 26(5), 711-723, doi: 10.1016/j.marpetgeo.2008.02.010.
672 Loncke, L., Gaullier, V., Droz, L., Ducassou, E., Migeon, S.,Mascle, J., 2009b. Multi-scale slope
673 instabilities along the Nile deep-sea fan, Egyptian margin: A general overview. Marine and
674 Petroleum Geology, 26(5), 633-646, doi: 10.1016/j.marpetgeo.2008.03.010.
675 Loncke, L., Gaullier, V., Mascle, J., Vendeville, B.,Camera, L., 2006. The Nile deep-sea fan: An example
676 of interacting sedimentation, salt tectonics, and inherited subsalt paleotopographic features.
677 Marine and Petroleum Geology, 23(3), 297-315, doi:DOI 10.1016/j.marpetgeo.2006.01.001.
678 Major, C., Ryan, W., Lericolais, G.,Hajdas, I., 2002. Constraints on Black Sea outflow to the Sea of
679 Marmara during the last glacial-interglacial transition. Marine Geology, 190(1-2), 19-34.
680 McAdoo, B.G., Pratson, L.F.,Orange, D.L., 2000. Submarine landslide geomorphology, US continental
681 slope. Marine Geology, 169(1-2), 103-136.
682 McHugh, C.M.G., Gurung, D., Giosan, L., Ryan, W.B.F., Mart, Y., Sancar, U., Burckle, L.,Çağatay, M.N.,
683 2008. The last reconnection of the Marmara Sea (Turkey) to the World Ocean: A
684 paleoceanographic and paleoclimatic perspective. Marine Geology, 255(1-2), 64-82, doi:
685 10.1016/j.margeo.2008.07.005.
686 McHugh, C.M.G., Seeber, L., Cormier, M.H., Dutton, J., Çağatay, N., Polonia, A., Ryan, W.B.F.,Görür,
687 N., 2006. Submarine earthquake geology along the North Anatolia Fault in the Marmara Sea,
688 Turkey: A model for transform basin sedimentation. Earth and Planetary Science Letters,
689 248(3-4), 661-684, doi: 10.1016/j.epsl.2006.05.038.
690 Menot, G.,Bard, E., 2010. Geochemical evidence for a large methane release during the last
691 deglaciation from Marmara Sea sediments. Geochimica Et Cosmochimica Acta, 74(5), 1537-
692 1550, doi: 10.1016/j.gca.2009.11.022.

693 Mienert, J., Vanneste, M., Bunz, S., Andreassen, K., Haflidason, H.,Sejrup, H.P., 2005. Ocean warming
694 and gas hydrate stability on the mid-Norwegian margin at the Storegga Slide. Marine and
695 Petroleum Geology, 22(1-2), 233-244, doi: 10.1016/j.marpetgeo.2004.10.018.
696 Mulder, T.,Cochonat, P., 1996. Classification of offshore mass movements. Journal of Sedimentary
697 Research, 66(1), 43-57.
698 Mulder, T., Gonthier, E., Lecroart, P., Hanquiez, V., Marches, E.,Voisset, M., 2009. Sediment failures
699 and flows in the Gulf of Cadiz (eastern Atlantic). Marine and Petroleum Geology, 26(5), 660-
700 672.
701 Okay, A.I., Demirbag, E., Kurt, H., Okay, N., Kuşçu, I., 1999. An active, deep marine strike-slip basin
702 along the North Anatolian fault in Turkey. Tectonics, 18, 129-147.
703 Okay, A., I., Tüysüz, O.,S., K., 2004. From transpression to transtension: changes in morphology and
704 structure around a bend on the North Anatolian Fault in the Marmara region.
705 Tectonophysics, 391(1-4), 259-282, doi:10.1016/j.tecto.2004.07.016.
706 Orange, D.L., Greene, H.G., Reed, D., Martin, J.B., McHugh, C.M., Ryan, W.B.F., Maher, N., Stakes,
707 D.,Barry, J., 1999. Widespread fluid expulsion on a translational continental margin: Mud
708 volcanoes, fault zones, headless canyons, and organic-rich substrate in Monterey Bay,
709 California. Geological Society of America Bulletin, 111(7), 992-1009.
710 Örgülü, G., 2011. Seismicity and source parameters for small-scale earthquakes along the splays of
711 the North Anatolian Fault (NAF) in the Marmara Sea. Geophysical Journal International,
712 184(1), 385-404, doi:10.1111/j.1365-246X.2010.04844.x.
713 Özeren, M.S., Çağatay, M.N., Postacioglu, N., Şengör, A.M.C., Görür, N.,Eris, K., 2010. Mathematical
714 modelling of a potential tsunami associated with a late glacial submarine landslide in the Sea
715 of Marmara. Geo-Marine Letters, 30(5), 523-539, doi:DOI 10.1007/s00367-010-0191-1.
716 Parke, J.R., Minshull, T.A., Anderson, G., White, R.S., McKenzie, D., Kuşçu, I., Bull, J.M., Görür, N.,
717 Şengör, C., 1999. Active faults in the Sea of Marmara, western Turkey, imaged by seismic
718 reflection profiles. Terra Nova, 11, 223-227.

719 Parke, J.R., White, R.S., McKenzie, D., Minshull, T.A., Bull, J., Kuşçu, I., Görür, N., Şengör, C., 2002.
720 Interaction between faulting and sedimentation in the sea of Marmara, western Turkey. J;
721 Geophys. Res., 107(B11), doi:10.1029/2001JB000450
722 Parsons, T., 2004. Recalculated probability of M >= 7 earthquakes beneath the Sea of Marmara,
723 Turkey. Journal of Geophysical Research-Solid Earth, 109(B5), B05304, doi:
724 10.1029/2003jb002667.
725 Piper, D.J.W., Pirmez, C., Manley, P.L., Long, D., Flood, R.D., Normark, W.R.,Showers, W., 1997. Mass-
726 transport deposits of the Amazon fan. In: R.D. Flood, D.J.W. Piper, A. Klaus,L.C. Peterson
727 (Editors), Proceedings of the Ocean Drilling Program, Scientific Results 155. College Station,
728 TX.
729 Polonia A., Cormier, M.H., Çagatay, M.N., Bortoluzzi, G., Bonatti, E., Gasperini, L., Seeber,L., Görür,
730 N., Capotondi, L., McHugh, C.M.G., Ryan, W.B.F., Emre, Ö., Okay, N., Ligi, M., Tok, B., Blasi, A.,
731 Busetti, M., Eris, K., Fabretti,P., Fielding, E.J., Imren, C., Kurt, H., Magagnoli, A., Marozzi, G.,
732 Ozer, N., Penitenti, D., Serpi, G., Sarikavak, K., 2002. Exploring submarine earthquake geology
733 in the Marmara Sea, EOS Transactions AGU, 83, 229 and 235-236.
734 Rangin, C., Le Pichon, X., Demirbag, E.,Imren, C., 2004. Strain localization in the Sea of Marmara:
735 Propagation of the North Anatolian Fault in a now inactive pull-apart. Tectonics, 23, TC2014,
736 doi:10.1029/2002TC001437.
737 Reichel, T.,Halbach, P., 2007. An authigenic calcite layer in the sediments of the Sea of Marmara--A
738 geochemical marker horizon with paleoceanographic significance. Deep Sea Research Part II:
739 Topical Studies in Oceanography, 54(11-13), 1201-1215.
740 Ryan, W.B.F., Major, C.O., Lericolais, G.,Goldstein, S.L., 2003. Catastrophic Flooding of the Black Sea.
741 Annu. Rev. Earth Planet. Sci., 31, 525-554.
742 Ryan, W.B.F., Pitman, W.C., Major, C.O., Shimkus, K., Moskalenko, V., Jones, G.A., Dimitrov, P., Görür,
743 N., Sakinc, M.,Yuce, H., 1997. An abrupt drowning of the Black Sea shelf. Marine Geology,
744 138(1-2), 119-126

745 Sato, T., Kasahara, J., Taymaz, T., Ito, M., Kamimura, A., Hayakawa, T.,Tan, O., 2004. A study of
746 microearthquake seismicity and focal mechanisms within the Sea of Marmara (NW Turkey)
747 using ocean bottom seismometers (OBSs). Tectonophysics, 391(1-4), 303-314,
748 doi:10.1016/j.tecto.2004.07.018.
749 Sanchez, G., Rolland, Y., Corsini, M., Braucher, R., Bourles, D., Arnold, M.,Aumaitre, G., 2010.
750 Relationships between tectonics, slope instability and climate change: Cosmic ray exposure
751 dating of active faults, landslides and glacial surfaces in the SW Alps. Geomorphology, 117(1-
752 2), 1-13, doi:10.1016/j.geomorph.2009.10.019.
753 Seeber, L., Cormier, M.H., McHugh, C., Emre, O., Polonia, A.,Sorlien, C., 2006. Rapid subsidence and
754 sedimentation from oblique slip near a bend on the North Anatolian transform fault in the
755 Marmara Sea, Turkey. Geology, 34(11), 933-936, doi: 10.1130/G22520a.1.
756 Seeber, L., Emre, O., Cormier, M.H., Sorlien, C.C., McHugh, C.M.G., Polonia, A., Ozer, N.,Çağatay, N.,
757 2004. Uplift and subsidence from oblique slip: the Ganosâ€“Marmara bend of the North
758 Anatolian Transform, western Turkey. Tectonophysics, 391(1-4), 239-258.
759 Şengör, A.M.C., 2011. Istanbul Boðazi niçin Boðaziçi'nde açilmiþtir? In: D. Ekinci (Editor), Fiziki
760 Cografya Araþtirmalari Sistematik ve Bolgesel- Profesör Doktor Mehmet Yildiz Hosgoren'e
761 Armagan, Türk, Cografya Kurumu Yayinlari, sayý 6, Istanbul, pp. 55-102.
762 Şengör, A.M.C., Görür, N.,Saroglu, F., 1985. Strike-slip faulting and related basin formation in zones
763 of tectonic escape : Turkey as a case study. In: K.T. Biddle,N.C. Blick (Editors), Strike-slip
764 deformation, basin formation and sedimentation. Soc. Econ. Paleon. Mine. Spec. Publication,
765 pp. 227-264.
766 Şengör, A.M.C., Tuysuz, O., Imren, C., Sakinc, M., Eyidogan, H., Görür, G., Le Pichon, X.,Rangin, C.,
767 2005. The North Anatolian Fault: A new look. Annual Review of Earth and Planetary Sciences,
768 33, 37-112.
769 Shillington, D.J., Seeber, L., Sorlien, C.C., Steckler, M.S., Kurt, H., Dondurur, D., Cifci, G., Imren, C.,
770 Cormier, M.H., McHugh, C.M.G., Gurcay, S., Poyraz, D., Okay, S., Atgin, O.,Diebold, J.B., 2012.

771 Evidence for widespread creep on the flanks of the Sea of Marmara transform basin from
772 marine geophysical data. Geology, 40(5), 439-442, doi:10.1130/g32652.1.
773 Stanley, D.J.,Blanpied, C., 1980. Late Quaternary Water Exchange between the Eastern
774 Mediterranean and the Black-Sea. Nature, 285(5766), 537-541.
775 Tary, J.B., Géli, L., Henry, P., Natalin, B., Gasperini, L., Comoglu, M., Çağatay, N.,Bardainne, T., 2011.
776 Sea-Bottom Observations from the Western Escarpment of the Sea of Marmara. Bulletin of
777 the Seismological Society of America, 101(2), 775-791, doi:10.1785/0120100014.
778 Tryon, M.D., Henry, P., Çağatay, M.N., Zitter, T.A.C., Géli, L., Gasperini, L., Burnard, P., Bourlange,
779 S.,Grall, C., 2010. Pore fluid chemistry of the North Anatolian Fault Zone in the Sea of
780 Marmara: A diversity of sources and processes. Geochemistry Geophysics Geosystems, 11,
781 Q0ad03 , doi: 10.1029/2010gc003177.
782 Tripsanas, E.K., Piper, D.J.W.,Campbell, D.C., 2008. Evolution and depositional structure of
783 earthquake-induced mass movements and gravity flows: Southwest Orphan Basin, Labrador
784 Sea. Marine and Petroleum Geology, 25(7), 645-662, doi: 10.1016/j.marpetgeo.2007.08.002.
785 Tur, H., 2007. An example of secondary fault activity along the north Anatolian Fault on the NE
786 Marmara Sea Shelf, NW Turkey. Earth Planets and Space, 59(6), 541-552.
787 Vidal, L., Menot, G., Joly, C., Bruneton, H., Rostek, F., Çağatay, M.N., Major, C.,Bard, E., 2010.
788 Hydrology in the Sea of Marmara during the last 23 ka: Implications for timing of Black Sea
789 connections and sapropel deposition. Paleoceanography, 25, Pa1205,
790 doi: 10.1029/2009pa001735.
791 Yalciner, A.C., Alpar, B., Altinok, Y., Ozbay, I.,Imamura, F., 2002. Tsunamis in the Sea of Marmara -
792 Historical documents for the past, models for the future. Marine Geology, 190(1-2), 445-463.
793 Yaltirak, C., 2002. Tectonic evolution of the Marmara Sea and its surroundings. Marine Geology,
794 190(1-2), 493-529.
795 Zitter, T.A.C., Henry, P., Aloisi, G., Delaygue, G., Çağatay, M.N., de Lépinay, B.M., Al-Samir, M.,
796 Fornacciari, F., Tesmer, M., Pekdeger, A., Wallmann, K.,Lericolais, G., 2008. Cold seeps along

the main Marmara Fault in the Sea of Marmara (Turkey). Deep-Sea Research Part I-Oceanographic Research Papers, 55(4), 552-570, doi: 10.1016/j.dsr.2008.01.002.

Figure legends

Figure 1: (a) Active tectonics of the eastern Mediterranean Sea showing the study area (SOM: Sea of Marmara) along the North Anatolian Fault. NAFZ: North Anatolian Fault Zone - EAFZ: East Anatolian Fault Zone - DSTFZ: Dead Sea Transform Fault Zone. (b) Multibeam backscatter image of the Sea of Marmara with simplified sketch of the North Anatolian fault system (modified after Le Pichon et al., 2001, Grall et al., 2012; see Fig. 3 for a detailed structural map). Insets indicate the location of Fig. 2, Fig. 4, Fig. 5, Fig. 6, Fig. 7, Fig. 8, and Fig. 9. Abbreviations are as follow: TB: Tekirdağ Basin; CB: Central Basin; KB: Kumburgaz Bain; CnB: Çınarcık Basin; WH: Western High; CH: Central High; GoG: Gulf of Gemlik; GoI: Gulf of Izmit; ImI: Imralı Island; AP: Armutlu Peninsula.

Figure 2: Characteristics of the mass wasting features within the different datasets: (a) slope gradient map showing curved slope failure scars, canyons, erosional gullies and slide toes; (b1) transparent, (b2) hummocky and (b3) hyperbolic chirp echo-characteristics corresponding to the mass wasting deposits; (c) sedimentary sequence within cores; (d) visual observation of avalanche debris deposits from Nautile dive.

Figure 3: Map of the mass wasting features, active faults, canyons and fluid seepage areas in the Sea of Marmara. Multibeam bathymetric data from Rangin et al. (2001), active faults modified after Le Pichon et al. (2003) and seepage sites modified after Zitter et al. (2008) and Géli et al. (2008).

Figure 4: (a) Shaded bathymetric and (b) slope gradient map of Çınarcık Basin, derived from EM300 multibeam data (38 m grid cell).

Figure 5: (a) Slope gradient map, derived from EM300 multibeam data (38 m grid cell), of the Tuzla Complex with the dive track and MTA seismic line location; in bold the section shown in (c). Slope gradient colour scale is the same as on Fig. 4. (b) Dive 1652 pictures of the Tuzla Complex headscarp showing outcrop of palaeozoic black shales with corals. (c) MTA multichannel seismic section

obtained on board the R/V Sismik1 (and processed by Caner Imren) across the Tuzla Landslide Complex, showing the rotational blocks and the headscarp. Modified after Özeren et al. (2010).

Figure 6: Shaded bathymetric map derived from multibeam EM300 data (38 m grid cell), dive track and dive pictures of Marnaut dive 1653 on the Yalova Complex, south of the Çınarcık Basin (location on Fig. 1) showing undraped chaotic blocks of authigenic carbonate crusts and evidence of fluid seepage (black patches and white bacterial mats). Bathymetric colour range is same as on Fig. 4.

Figure 7: Marmarascarps profile (3.5kHz frequency) across the base of the northern Çınarcık slope where scree is observed on seafloor pictures (chaotic blocks and fallen boulders). The scree at the base of the cliff is also observed on the bathymetric data (orange area). Red stars indicate the location of recognised fluid seepages from Nautile and ROV observations (black reduced sediments patches with white bacterial mats).

Figure 8: (a) Shaded bathymetric map (colour range is same as on Fig. 4), (b) slope gradient map and (c) slope-facing map (aspect map) of the Ganos Landslide Complex in the Tekirdağ Basin, derived from multibeam EM300 data with a grid cell resolution of 38 m. Aspect is the direction of maximum slope gradient, and slope gradient is the dip for each grid cell based on the elevation of its nearest neighbors. (d) The morpho-structural sketch (canyons in purple, landslides and slope failures in grey and faults in red) is interpreted from multibeam and backscatter data, and the active structures are modified after Le Pichon et al. (2003). (e) Topographic profile along the major slope. Note the small staircase-like scarps perpendicular to the slope, interpreted as creep (see Shillington et al., 2012), and the multiple slope failures in the upper part of the slide, on the extremity of Ganos fault segment.

Figure 9: (a) Shaded relief map of Tekirdağ Basin with location of chirp lines and cores. Inset indicates the location of (b): Slope gradient map zoomed on the canyons showing scars on the flanks and within the thalweg. Slope gradient colour scale is the same as on Fig. 4. White coloured lines are 5 m isobaths. (c) Marnaut 16 chirp profile (3.5 kHz frequency) across a canyon showing the infill of the canyon.

Figure 10: Lithology and sedimentary sequence interpretation for cores MD042737 and MD042740 (Marion Dufresne calypso cores) and MNTKS30 (Marnaut kullenberg core) in the Tekirdağ Basin, at the mouth of the canyon (see Fig. 9 for location). Detailed sections of the cores are illustrated with photographs and Scopix XRay images.

Figure 11: Marnaut 95 chirp profile (frequency of 3.5 kHz) in the Tekirdağ Basin showing a buried submarine landslide (transparent lens) intercalated within sediments. For location, see Fig. 9. The correlation of the strong reflective horizons (also noted a,b,c and d in Fig. 11 in Zitter el al. 2008) with the core MD042737 indicates that this submarine landslide must have occurred at the beginning of marine stage in the Sea of Marmara.

Figure 12: (a) Micro-seismicity records from Sato et al. (2004), Karabulut et al. (2002) and Örgülü et al. (2011) projected on multibeam shaded relief map of Çınarcık Basin, including the Tuzla and Yalova complexes with focal mechanisms modified after Karabulut et al. (2002), (compressional quadrants in red). (b) Micro-seismicity records from Sato et al. (2004) and Örgülü et al. (2011) projected on multibeam shaded relief map of Tekirdağ Basin, including the Ganos Complex.

Table 1: Table presenting the mean slope gradient of the main margins and major submarine landslides determined within polygons defined in areas of similar steepness and centered at the indicated longitude and latitude.

Table 2: Table summarizing the mass wasting features presented within this study and mapped in Fig. 3, with their location, their name or context, their surface, length and width, their age known from this study or from the literature and the inferred processes that generate them. References to studies dealing with some of these mass wasting features are indicated within this table with numbers as follows: 1: Gazioğlu et al., 2002; 2: Gazioğlu et al., 2005; 3: Tur, 2007; 4: Gökçeoğlu et al., 2009; 5: Görür and Çağatay, 2010; 6: Özeren et al., 2010; 7: Shillington et al., 2012.

Location	Slope average (°)	Number of cells	Area (km2)	Center longitude	Center latitude
Slopes:					
NE Tekirdag	19.25	26622	38.81	27° 28' 49.45" E	40° 50' 6.69" N
N Tekirdag	8.21	56081	83.10	27° 40' 59.25" E	40° 53' 52.88" N
S Tekirdag	7.93	146414	216.20	27° 32' 10.89" E	40° 44' 46.93" N
W Western High	7.93	36635	53.93	27°42' 8.26" E	40°49' 16.79" N
E Western High	7.17	12783	18.80	27°53' 37.07" E	40°49' 9.47" N
N Central Basin	11.45	100173	147.60	28° 3' 44.35" E	40° 54' 50.78" N
S Central Basin	8.34	126747	186.44	27° 59' 21.21" E	40° 43' 29.13" N
SE Central Basin	4.00	70431	103.61	28°9' 19.65" E	40°47' 58.86" N
N Kumburgaz	5.30	186127	275.23	28°21' 6.50" E	40°54' 3.36" N
S Kumburgaz	4.35	38823	57.08	28°22' 13.24" E	40°47' 48.42" N
W Central High	2.68	21818	32.09	28°29' 9.98" E	40°50' 57.84" N
E Central High	3.69	103781	155.48	28°40' 30.36" E	40°49' 20.07" N
NW Cinarcik	15.87	45535	69.15	28°47' 15.86" E	40°53' 36.72" N
N Cinarcik	23.11	34257	50.42	29° 1' 54.38" E	40° 49' 21.56" N
S Cinarcik	11.84	111849	164.89	28° 57' 44.04" E	40° 42' 14.78" N
SE Cinarcik	17.28	33830	49.75	29° 6' 34.60" E	40° 41' 2.90" N
Mass wasting features:					
S Ganos landslide	5.65	40677	60.16	27° 27' 52.22" E	40° 45' 9.78" N
N Ganos landslide	9.42	15912	23.40	27°26' 57.03" E	40° 46' 48.37" N
Tuzla landslide headscarp	21.04	4644	6.84	29° 14' 46.26" E	40° 45' 2.08" N
E Tuzla landslide	14.44	9130	13.39	27° 28' 2.65" E	40° 45' 30.56" N
Mass feature 32	10.14	16046	23.63	29°19' 1.25" E	40°42' 42.36" N

	Location	Context	Longitude	Latitude	Area (km2)	Length (km)	Width (km)	Age	References	Processes
1	Tekirdağ	Ganos Complex	27°27' 42.43" E	40°45' 28.60" N	84.9057	13.22	7.693		1,2,4,5,7	Creep and collapse (7) Deep seated gravitational (this study)
2	Tekirdağ	Ganos Complex	27°26' 39.06" E	40°45' 40.78" N	8.9333	6.24	1.036			Debris flow (this study)
3	Tekirdağ	Ganos Complex-Scar	27°25' 16.66" E	40°46' 18.83" N	0.5523	0.872	0.487			
4	Tekirdağ	Ganos Complex-Scar	27°25' 36.10" E	40°46' 19.99" N	1.0480	0.573	1.772			
5	Tekirdağ	Marmara Island Complex	27° 35' 54.76" E	40° 46' 57.44" N	15.3625	4.561	4.359		1,2,5	Creep (7)
6	Tekirdağ	Canyon	27°37' 22.39" E	40°47' 48.02" N	2.2270	-	-			
7	Central	Canyon	27°42' 21.92" E	40°42' 53.30" N	1.3642	-	-			
8	Western Ridge	W Western Ridge	27°42' 59.45" E	40°50' 12.04" N	9.8814	4.353	5.087	14 cal. ka (this study)	7	Creep (7), Debris flow (this study)
9	Western Ridge	W Western Ridge	27°44' 6.92" E	40°51' 11.92" N	1.7028	3.576	3.802		7	Creep (7)
10	Western Ridge	N Western ridge	27°47' 12.65" E	40°52' 35.88" N	0.6140	1.486	0.859		7	Creep (7)
11	Central	Canyon	27°44' 48.93" E	40°43' 7.28" N	1.3400	-	-			
12	Central	Canyon	27°46' 16.28" E	40°44' 46.10" N	2.5985	-	-			
13	Central	canyon	27°46' 4.69" E	40°42' 20.69" N	0.9638	-	-			
14	Central	canyon	27°48' 30.45" E	40°44' 12.80" N	0.2344	-	-			
15	Central	Canyon	27°49' 43.86" E	40°46' 14.00" N	0.6077	-	-			
16	Central	Canyon	27°50' 16.98" E	40°43' 1.46" N	0.8186	-	-			
17	Central	Canyon	27°51' 34.04" E	40°45' 13.43" N	4.1227	-	-			
18	Central	South Central	27°52' 42.52" E	40°46' 46.36" N	12.8765	3.23	4.154			
19	Central	Canyon	27°53' 48.99" E	40°44' 35.92" N	8.4838	-	-			
20	Central	E Western Ridge	27°54' 54.02" E	40°49' 33.17" N	11.4045	2.13	5.887			
21	Central	Canyon	27°55' 14.34" E	40°43' 50.69" N	0.6989	-	-			

22	Central	NE Central basin	28°10' 4.15" E	40°53' 28.66" N	24.1570	7.644	3.308		5	
23	Central	flank NE Central	28°8' 8.51" E	40°50' 1.98" N	2.7964	1.723	3.924		7	Creep (7)
24	Central Ridge	S Kumburgaz	28°23' 53.46" E	40°47' 51.77" N	29.6489	3.456	9.613		7	Creep (7)
25	Central Ridge	E Central Ridge	28°38' 45.58" E	40°48' 22.04" N	58.0094	11. 695	11.182		2,7	Creep (7)
26	Central Ridge	E Central Ridge	28°41' 52.62" E	40°51' 41.97" N	8.4042	6.07	3.899		7	Creep (7)
27	Çınarcık	South Çınarcık	29°01' 24.71" E	40°43' 7.74" N	118.8027	5.67	26.75		7	Creep (7)
28	Çınarcık	N Çınarcık scree slope	29°05' 32.77" E	40°46' 47.91" N	20.0913	-	-			
29	Çınarcık	South East Çınarcık	29°10' 46.37" E	40°41' 48.88" N	21.0210	3.52	5.85		5	
30	Çınarcık	Tuzla Complex	29°13' 27.30" E	40°45' 2.48" N	39.3684	5.681	6.44	17 ka (6)	1,2,3,4, 5,6,7	Deep-seated rotational (4,5, this study)
31	Çınarcık	South East Çınarcık	29°14' 11.81" E	40°41' 39.76" N	11.4806	5.287	2.193			
32	Çınarcık	Izmit Gulf	29°19' 22.42" E	40°42' 29.12" N	33.5267	8.468	4.753			

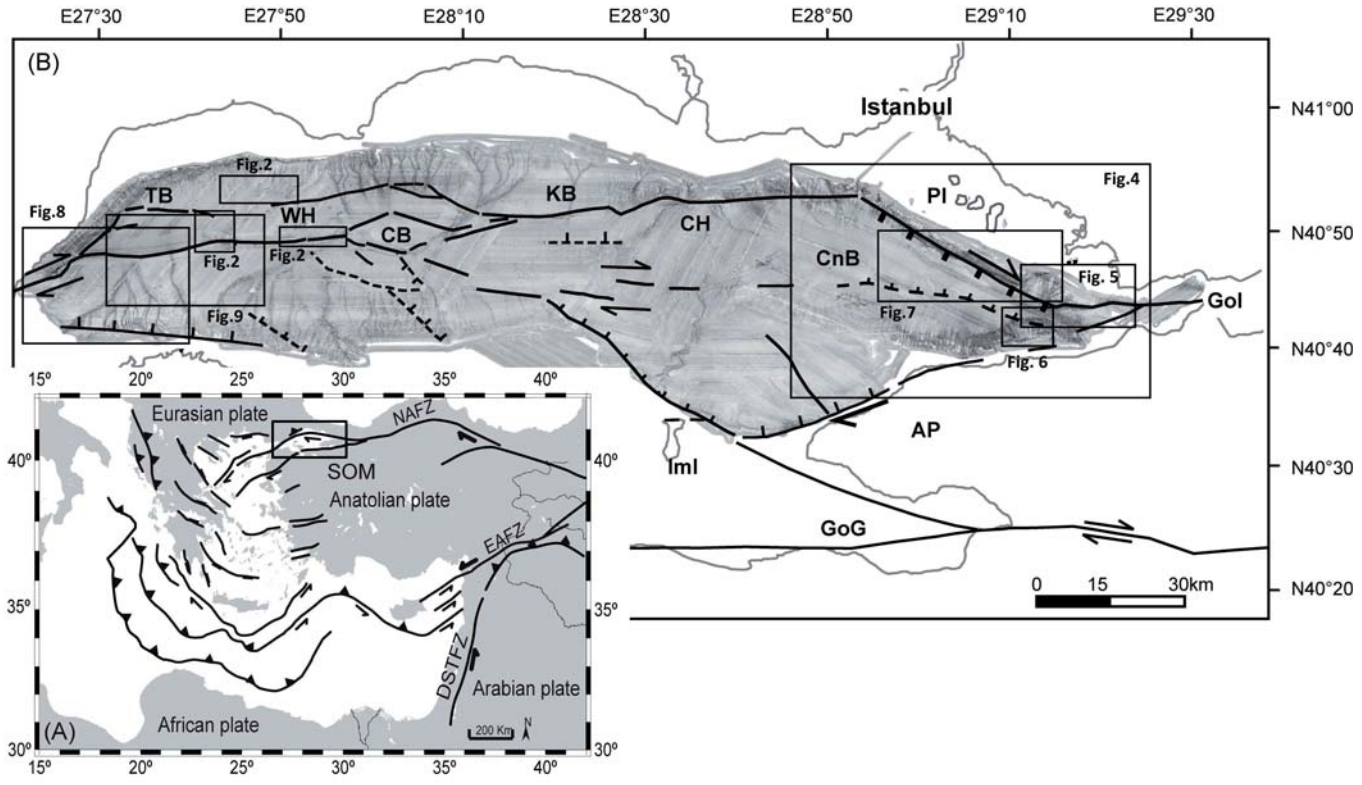
E27°30
E27°50
E28°10
E28°30
E28°50
E29°10
E29°30
(B)
Istanbul
N41°00
N40°50
N40°40
N40°30
N40°20
Fig.2
Fig.8
TB
WH
CB
KB
CH
PI
Fig.4
CnB
Fig. 5
Fig.7
Gol
Fig.9
Fig. 6
AP
Iml
GoG
0 15 30km
15°
20°
25°
30°
35°
40°
Eurasian plate
NAFZ
SOM
Anatolian plate
EAFZ
DSTFZ
Arabian plate
African plate
(A)
200 Km
N

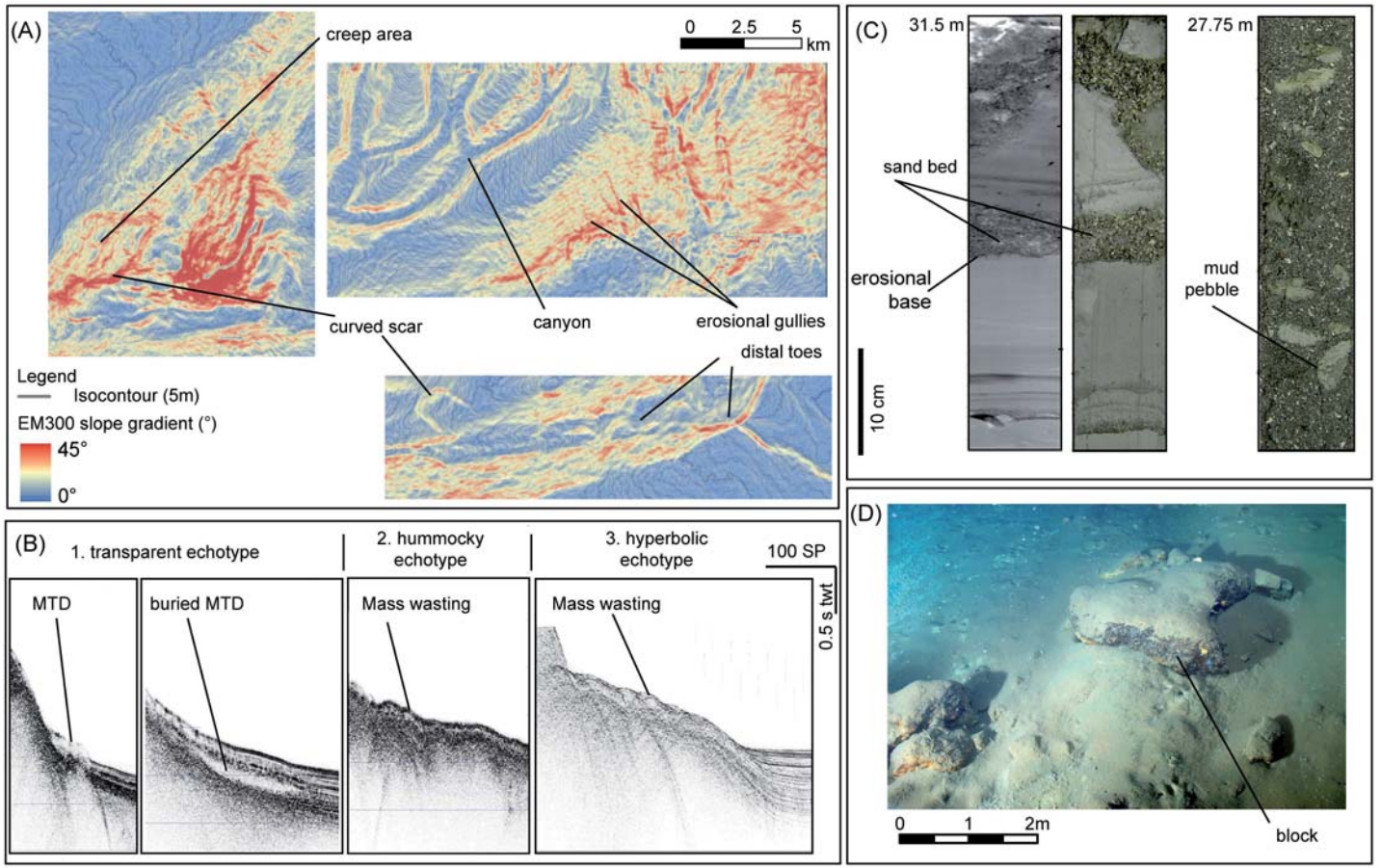
(A)
creep area
0 2.5 5
km
curved scar
canyon
erosional gullies
distal toes
Legend
Isocontour (5m)
EM300 slope gradient (°)
45°
0°
(B)
1. transparent echotype
2. hummocky echotype
3. hyperbolic echotype
100 SP
0.5 s twt
MTD
buried MTD
Mass wasting
Mass wasting
(C)
31.5 m
27.75 m
sand bed
erosional base
mud pebble
10 cm
(D)
0 1 2m
block

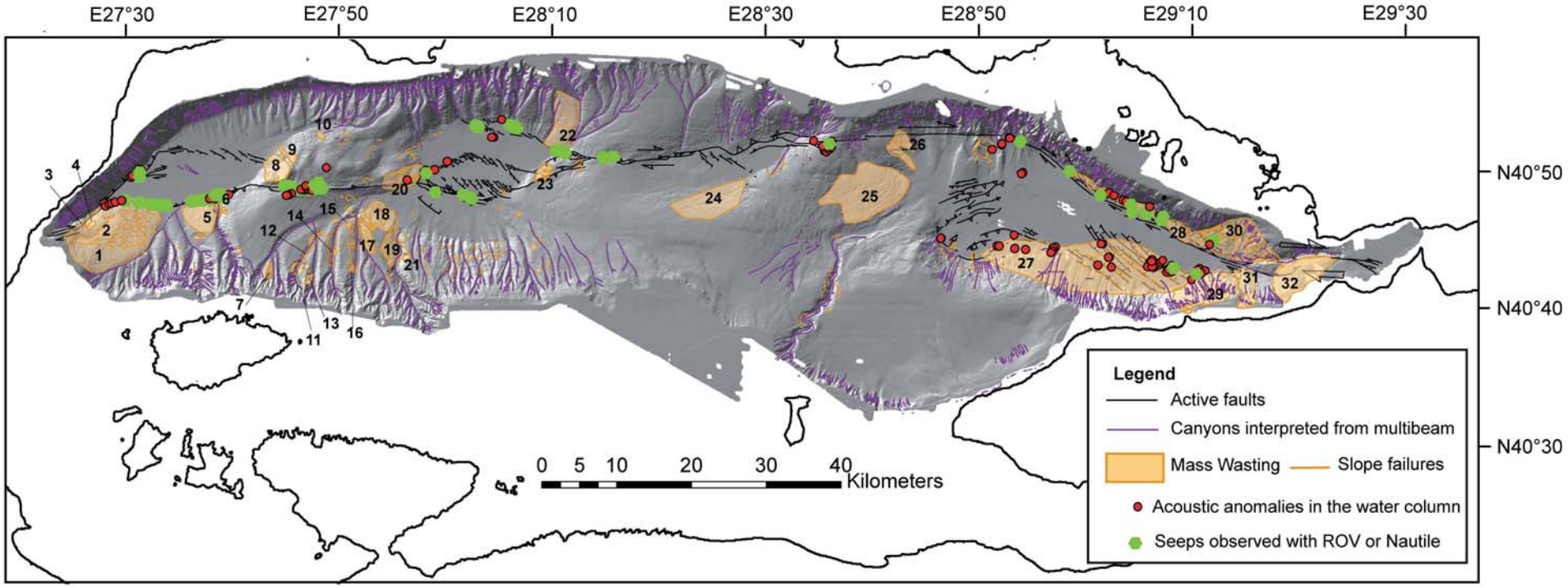
E27°30
E27°50
E28°10
E28°30
E28°50
E29°10
E29°30
N40°50
N40°40
N40°30
1
2
3
4
5
6
7
8
9
10
11
12
13
14
15
16
17
18
19
20
21
22
23
24
25
26
27
28
29
30
31
32
0 5 10 20 30 40
Kilometers
Legend
Active faults
Canyons interpreted from multibeam
Mass Wasting
Slope failures
Acoustic anomalies in the water column
Seeps observed with ROV or Nautile

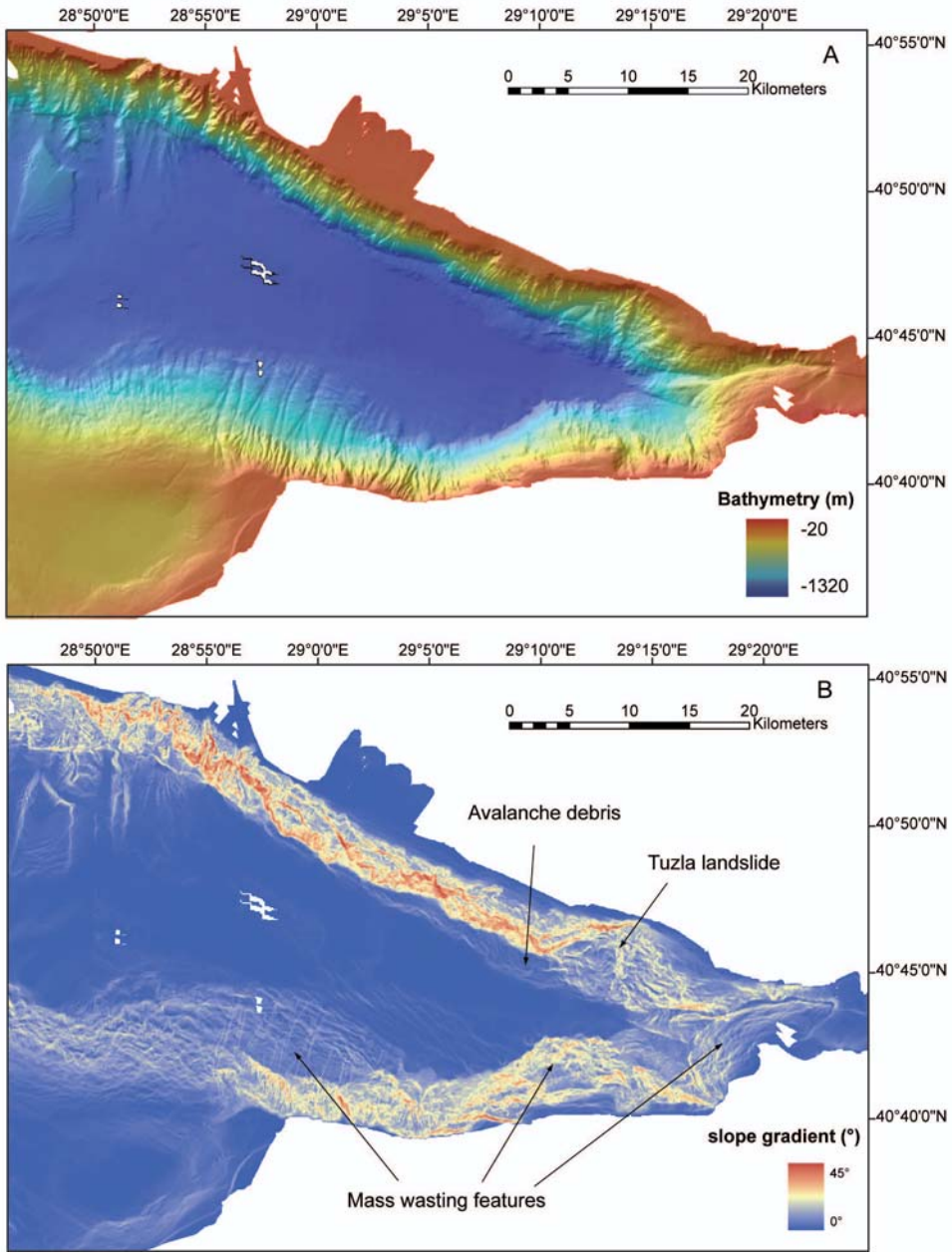
28°50'0"E
28°55'0"E
29°0'0"E
29°5'0"E
29°10'0"E
29°15'0"E
29°20'0"E
40°55'0"N
40°50'0"N
40°45'0"N
40°40'0"N
A
0 5 10 15 20
Kilometers
Bathymetry (m)
-20
-1320
B
Avalanche debris
Tuzla landslide
Mass wasting features
slope gradient (°)
45°
0°

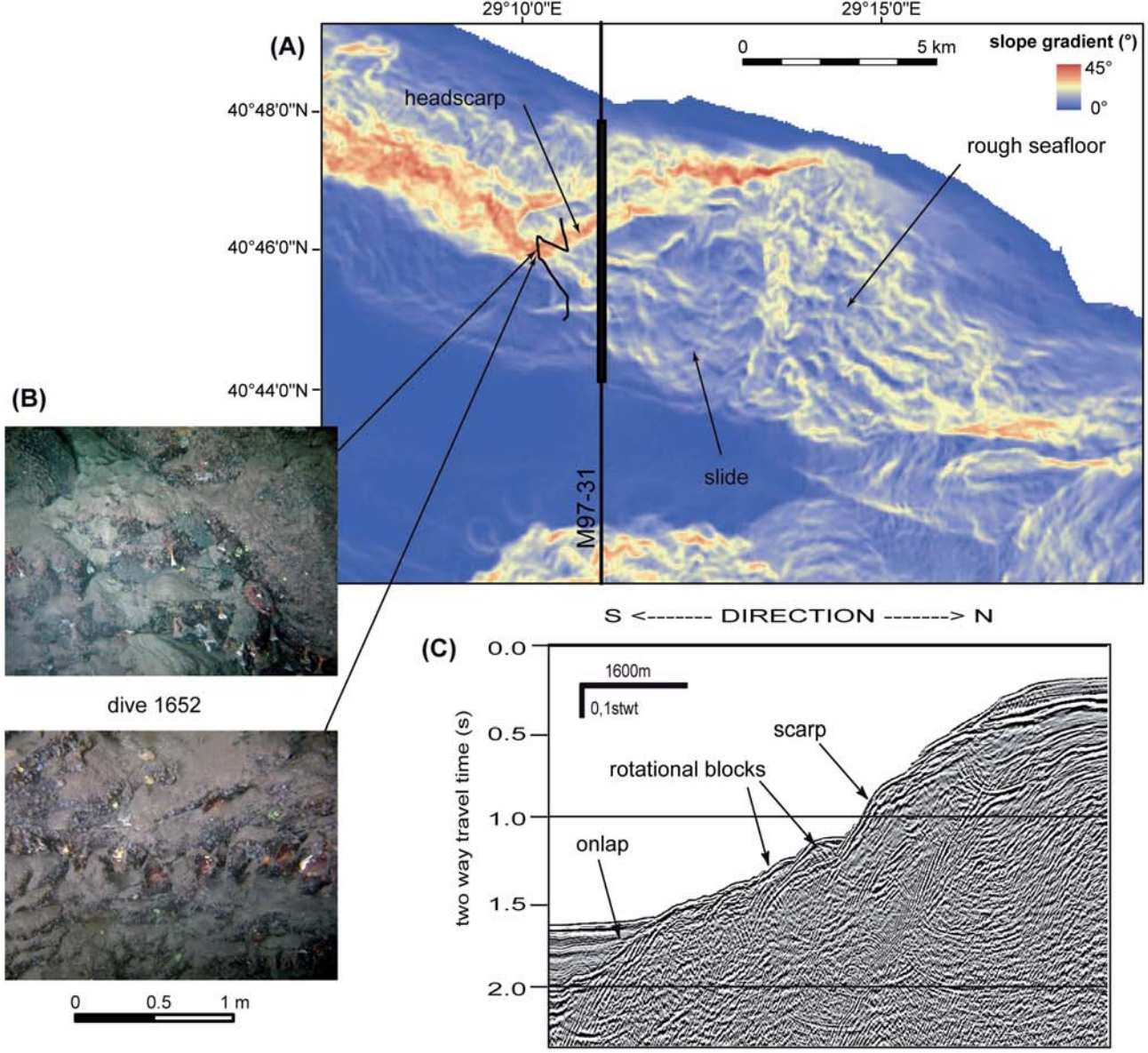
(A)
29°10'0"E
29°15'0"E
40°48'0"N
40°46'0"N
40°44'0"N
0
5 km
slope gradient (°)
45°
0°
headscarp
rough seafloor
slide
M97-31
(B)
dive 1652
0
0.5
1 m
S <------- DIRECTION -------> N
(C)
1600m
0,1stwt
scarp
rotational blocks
onlap
two way travel time (s)
0.0
0.5
1.0
1.5
2.0

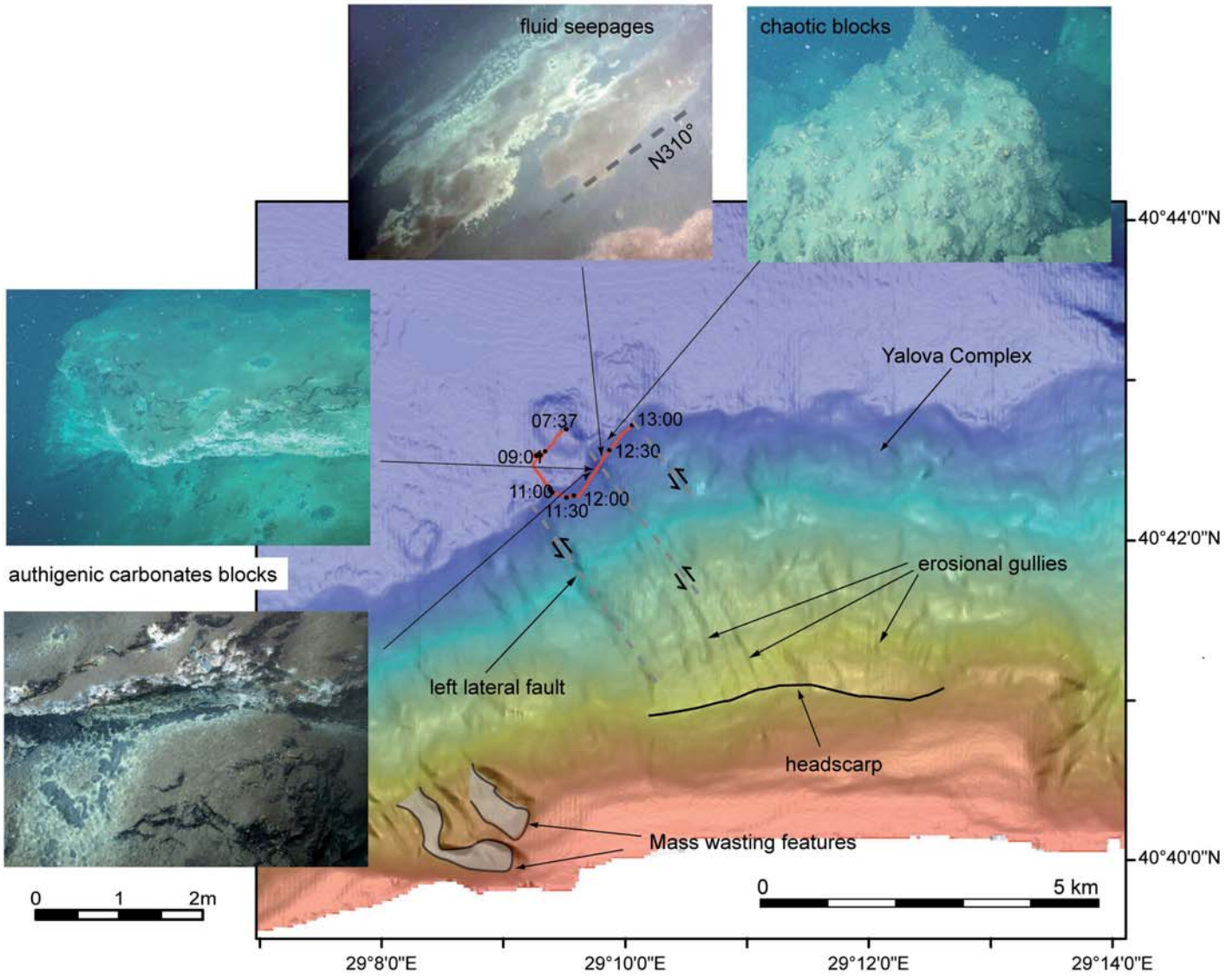
fluid seepages
N310°
chaotic blocks
authigenic carbonates blocks
Yalova Complex
07:37
09:0
11:00
11:30
12:00
12:30
13:00
erosional gullies
left lateral fault
headscarp
Mass wasting features
0 1 2m
0 5 km
40°44'0"N
40°42'0"N
40°40'0"N
29°8'0"E
29°10'0"E
29°12'0"E
29°14'0"E

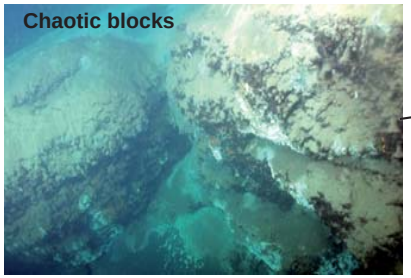
Chaotic blocks

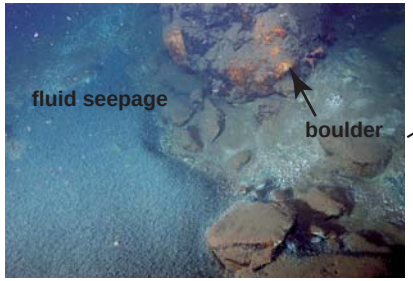
fluid seepage
boulder

0 1 2m

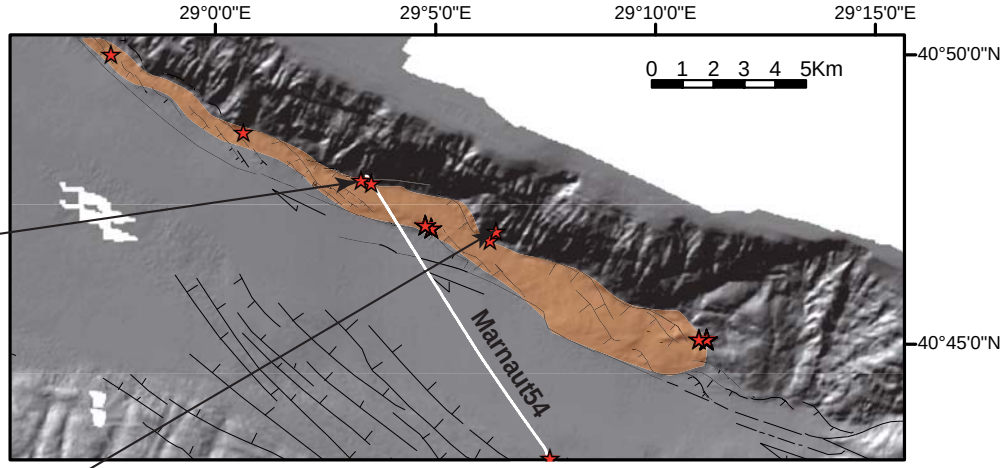
29°0'0"E
29°5'0"E
29°10'0"E
29°15'0"E
40°50'0"N
40°45'0"N
0 1 2 3 4 5Km
Marnaut54

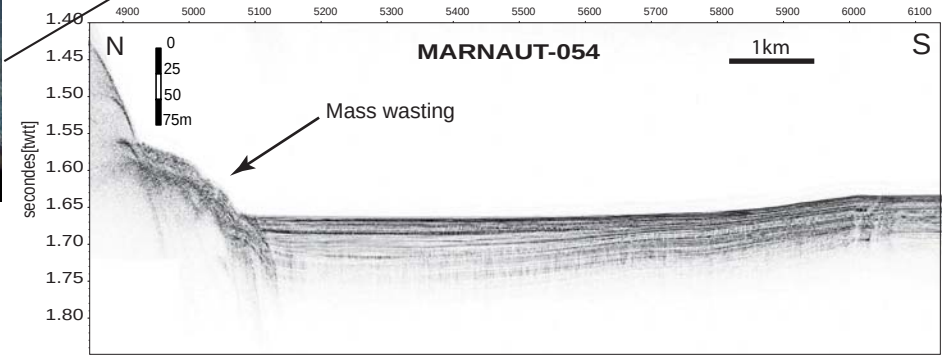
4900 5000 5100 5200 5300 5400 5500 5600 5700 5800 5900 6000 6100
1.40
1.45
1.50
1.55
1.60
1.65
1.70
1.75
1.80
secondes[twtt]
N
0
25
50
75m
MARNAUT-054
1km
S
Mass wasting

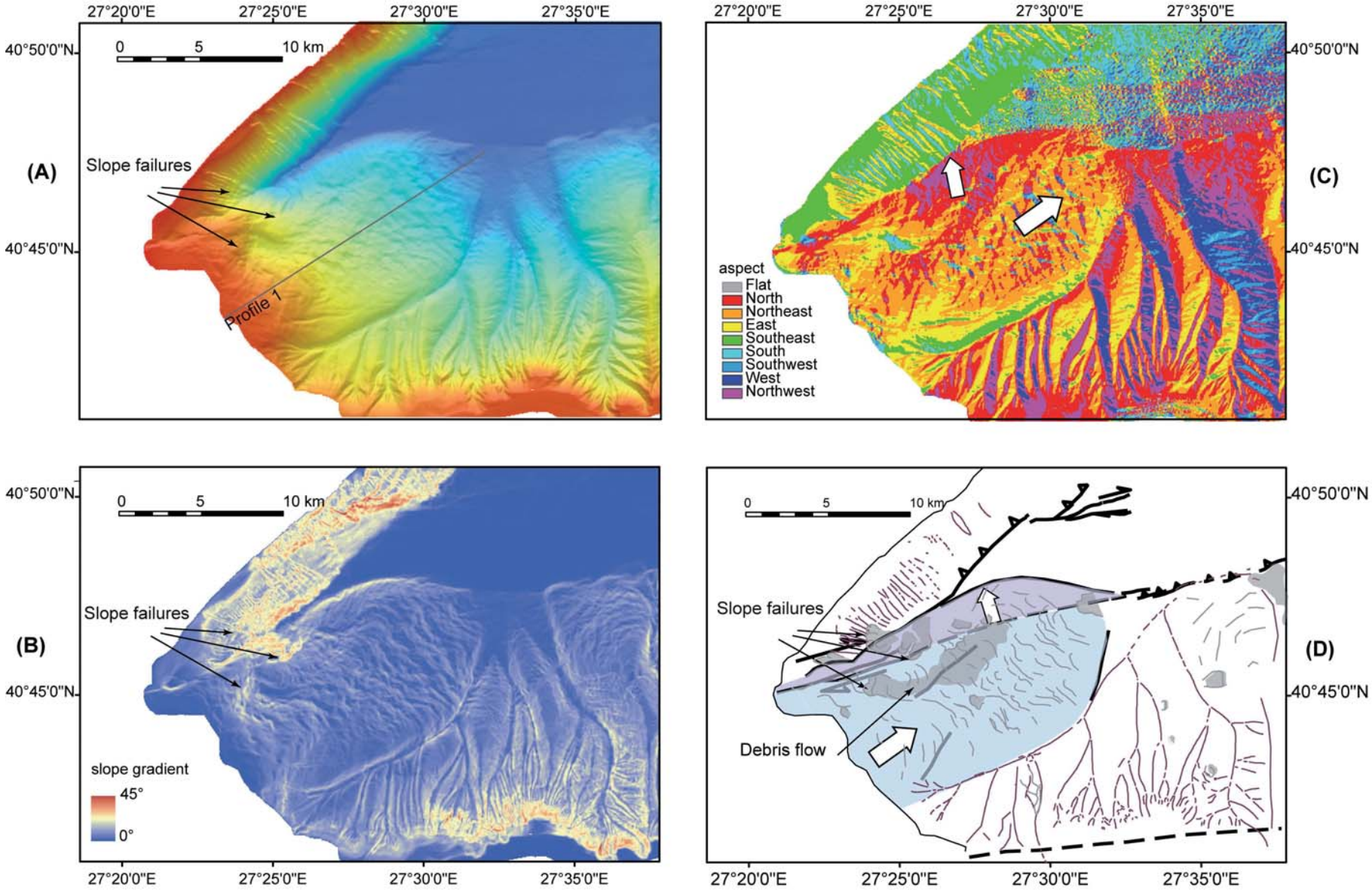
27°20'0"E
27°25'0"E
27°30'0"E
27°35'0"E
40°50'0"N
40°45'0"N
0 5 10 km
(A)
Slope failures
Profile 1
(C)
aspect
Flat
North
Northeast
East
Southeast
South
Southwest
West
Northwest
(B)
slope gradient
45°
0°
(D)
Debris flow
Profile 1
Distance (Km)
Depth (m)
0
-200
-400
-600
-800
-1000
-1200
0 2 4 6 8 10 12 14 16 18 20
(E)

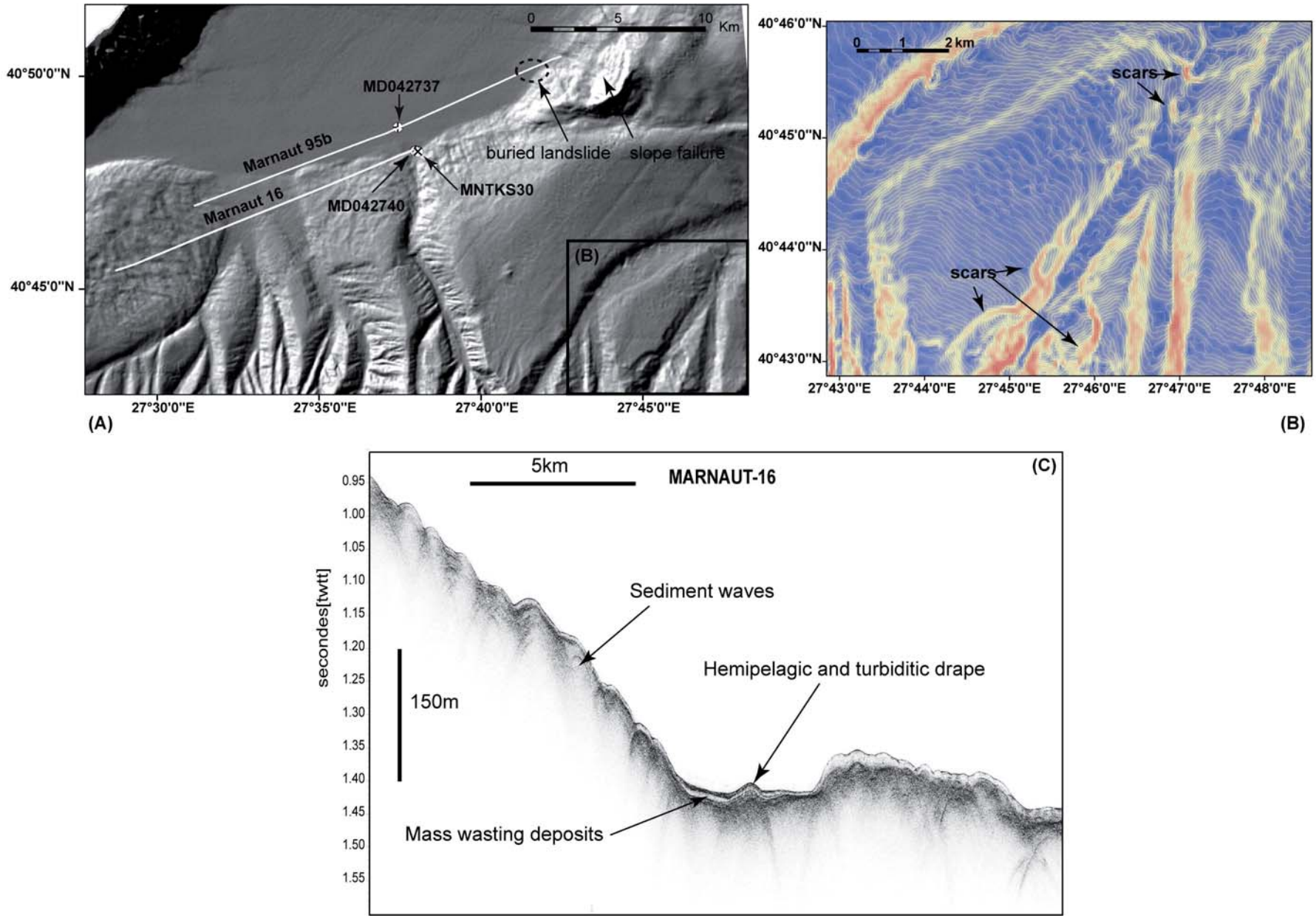
0 5 10 Km
40°50'0"N
40°45'0"N
MD042737
Marnaut 95b
Marnaut 16
MD042740
MNTKS30
buried landslide
slope failure
(B)
27°30'0"E
27°35'0"E
27°40'0"E
27°45'0"E
(A)
40°46'0"N
40°45'0"N
40°44'0"N
40°43'0"N
0 1 2 km
scars
scars
27°43'0"E
27°44'0"E
27°45'0"E
27°46'0"E
27°47'0"E
27°48'0"E
(B)
5km
MARNAUT-16
(C)
secondes[twtt]
0.95
1.00
1.05
1.10
1.15
1.20
1.25
1.30
1.35
1.40
1.45
1.50
1.55
Sediment waves
Hemipelagic and turbiditic drape
150m
Mass wasting deposits

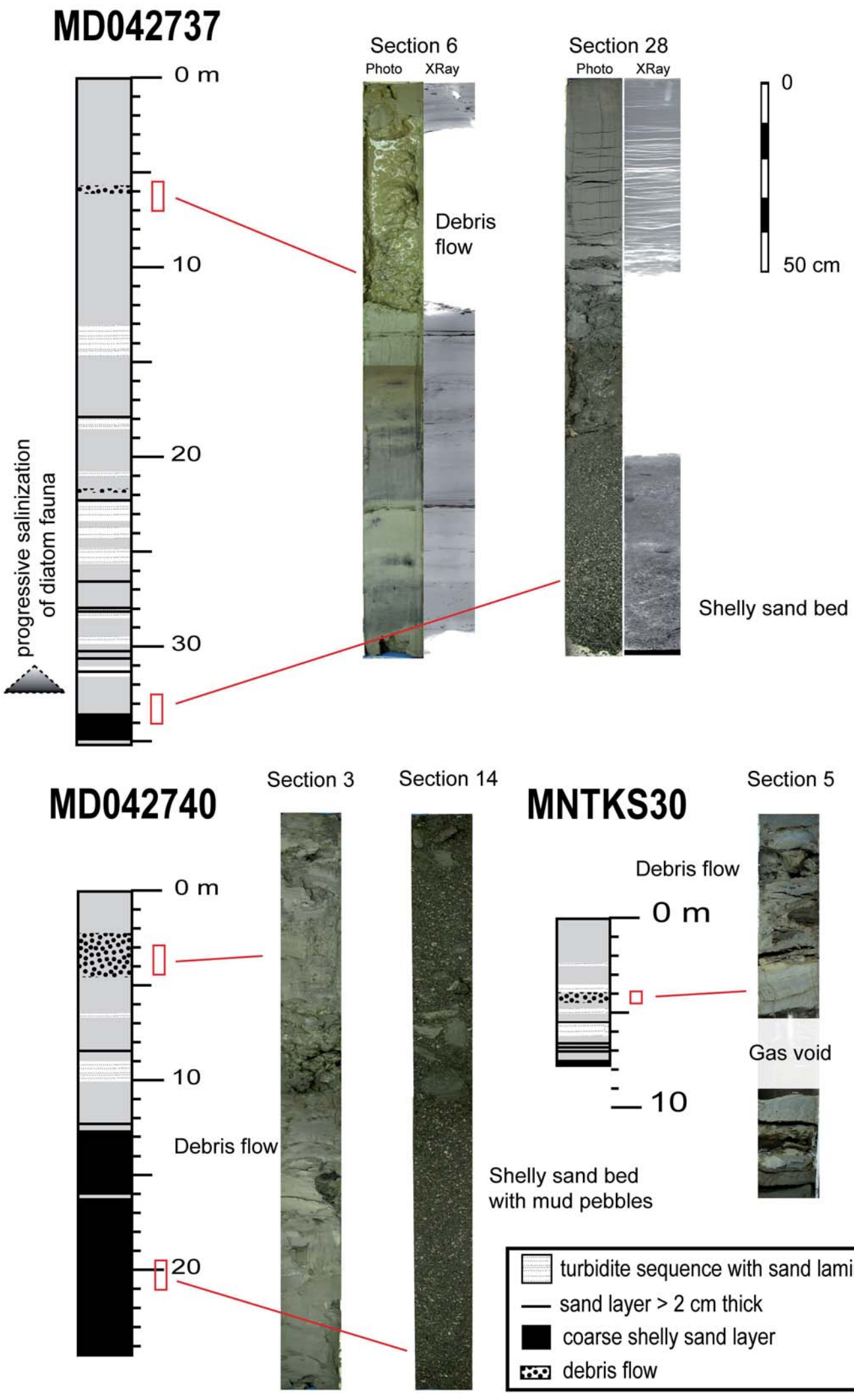
MD042737
Section 6
Photo
XRay
Section 28
Photo
XRay
0
50 cm
0 m
10
20
30
progressive salinization
of diatom fauna
Debris
flow
Shelly sand bed
MD042740
Section 3
Section 14
0 m
10
20
Debris flow
MNTKS30
Section 5
Debris flow
0 m
10
Gas void
Shelly sand bed
with mud pebbles
turbidite sequence with sand laminae
sand layer > 2 cm thick
coarse shelly sand layer
debris flow

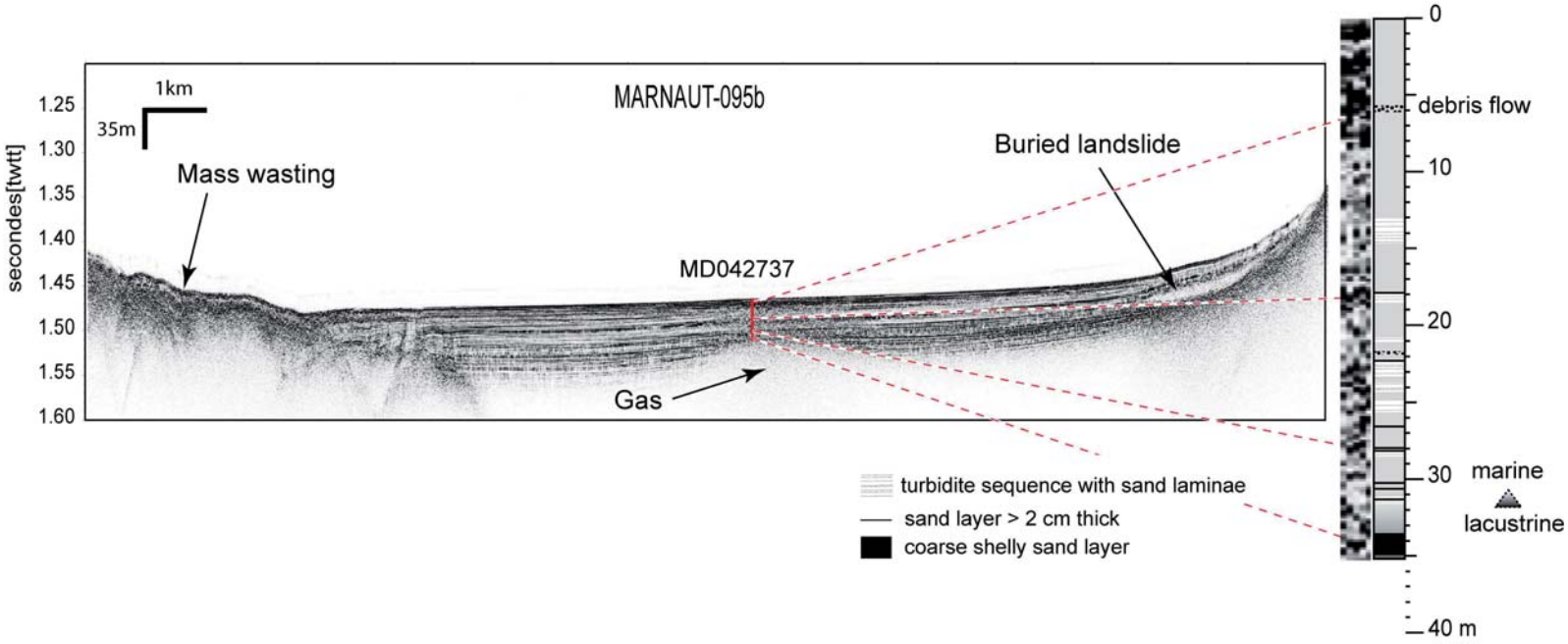
1km
35m
MARNAUT-095b
secondes[twtt]
1.25
1.30
1.35
1.40
1.45
1.50
1.55
1.60
Mass wasting
Buried landslide
MD042737
Gas
turbidite sequence with sand laminae
sand layer > 2 cm thick
coarse shelly sand layer
0
debris flow
10
20
30
marine
lacustrine
40 m

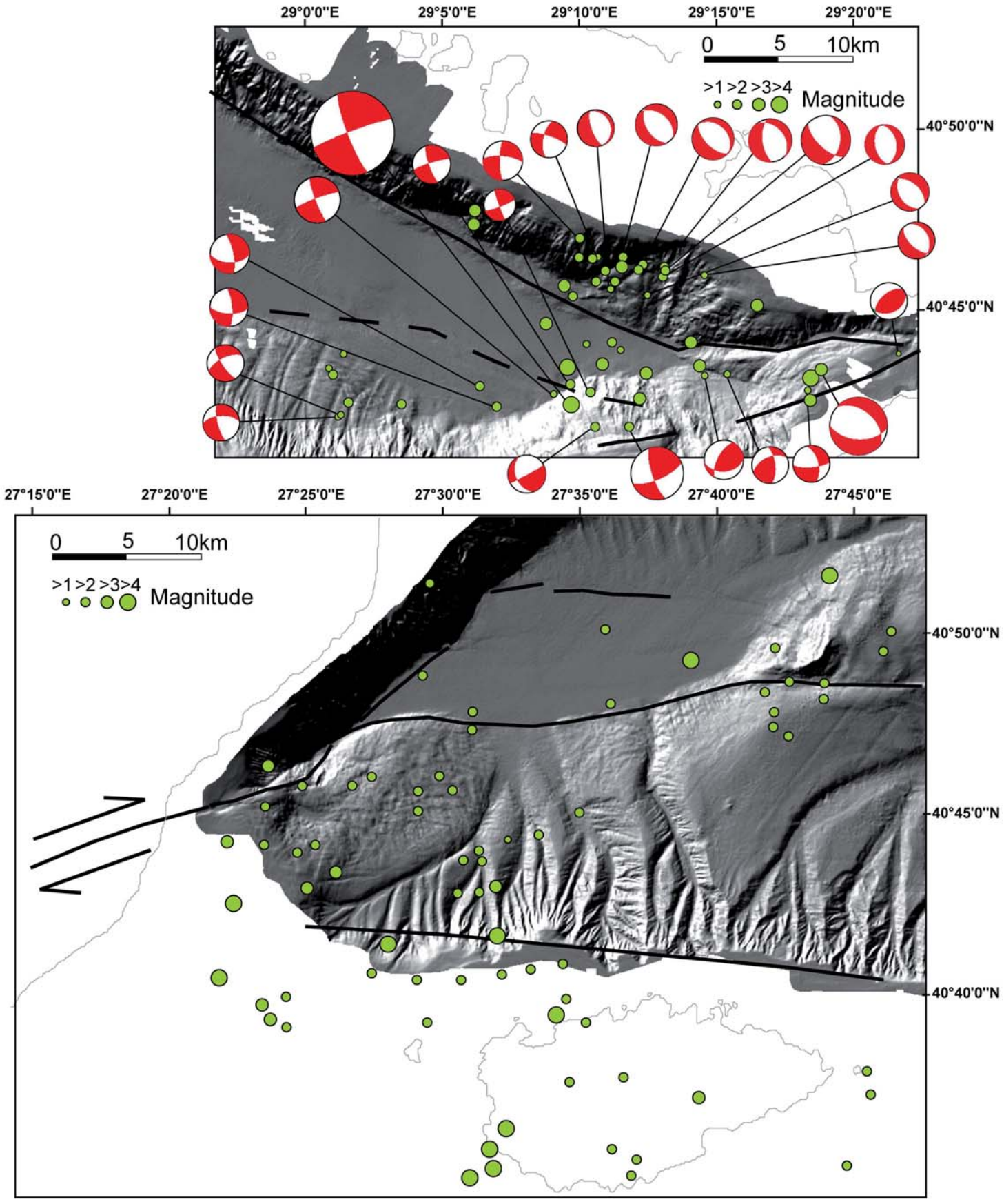
29°0'0"E
29°5'0"E
29°10'0"E
29°15'0"E
29°20'0"E
0 5 10km
>1 >2 >3>4 Magnitude
40°50'0"N
40°45'0"N
27°15'0"E
27°20'0"E
27°25'0"E
27°30'0"E
27°35'0"E
27°40'0"E
27°45'0"E
0 5 10km
>1 >2 >3>4 Magnitude
40°50'0"N
40°45'0"N
40°40'0"N